Draft version January 19, 2013
Preprint typeset using LaTeX style emulateapj v. 8/13/10

arXiv:1104.0681v2 [astro-ph.CO] 23 Sep 2011

# OUTFLOWING GALACTIC WINDS IN POST-STARBURST AND AGN HOST GALAXIES AT $0.2 < Z < 0.8$

Alison L. Coil[1,2], Benjamin J. Weiner[3], Daniel E. Holz[4], Michael C. Cooper[5,6], Renbin Yan[7], James Aird[1]

*Draft version January 19, 2013*

## ABSTRACT

We present Keck/LRIS-B spectra for a sample of ten AEGIS X-ray AGN host galaxies and thirteen post-starburst galaxies from SDSS and DEEP2 at $0.2 < z < 0.8$ in order to investigate the presence, properties, and influence of outflowing galactic winds at intermediate redshifts. We focus on galaxies that either host a low-luminosity AGN or have recently had their star formation quenched to test whether these galaxies have winds of sufficient velocity to potentially clear gas from the galaxy. We find, using absorption features of Fe II, Mg II, and Mg I, that six of the ten (60%) X-ray AGN host galaxies and four of the thirteen (31%) post-starburst galaxies have outflowing galactic winds, with typical velocities of $\sim 200$ km s$^{-1}$. We additionally find that most of the galaxies in our sample show line emission, possibly from the wind, in either Fe II* or Mg II. A total of 100% of our X-ray AGN host sample (including four red sequence galaxies) and 77% of our post-starburst sample has either blueshifted absorption or line emission. Several K+A galaxies have small amounts of cool gas absorption at the systemic velocity, indicating that not all of the cool gas has been expelled. We conclude that while outflowing galactic winds are common in both X-ray low-luminosity AGN host galaxies and post-starburst galaxies at intermediate redshifts, the winds are likely driven by supernovae (as opposed to AGN) and do not appear to have sufficiently high velocities to quench star formation in these galaxies.

*Subject headings:* galaxies: high-redshift – galaxies: evolution – galaxies: ISM – galaxies: active – galaxies: starburst – ultraviolet: ISM

## 1. INTRODUCTION

Galaxy redshift surveys have revealed that the optical restframe color distribution of galaxies is bimodal in both the local and distant Universe, beyond $z = 2$ (e.g., Strateva et al. 2001; Blanton et al. 2003; Faber et al. 2007; Kriek et al. 2008). Galaxies predominantly lie either along the "red sequence", which is composed of mostly quiescent, early-type galaxies, or in the "blue cloud" of star-forming, late-type galaxies. From $z = 1$ to today, the red sequence has roughly doubled in mass (Bell et al. 2004; Bundy et al. 2006; Brown et al. 2007; Faber et al. 2007), presumably as galaxies have moved from the blue cloud to the red sequence as a result of ending star formation and passively evolving. It is not yet understood what causes galaxies to stop forming stars, nor why their star formation remains quenched, i.e. why they do not continue to accrete additional gas and resume star formation.

One popular proposed mechanism for quenching star formation is gas blowout by a starburst and/or AGN, resulting from a merger event (e.g. Sanders et al. 1988; Hopkins et al. 2005). In this picture, the starburst and/or AGN is activated by gas inflow during the merger, and this subsequently drives an outflowing wind that fully clears gas from the galaxy, leading to the creation of a quiescent elliptical. A remaining low-luminosity AGN may provide a second mode of feedback and deter further star formation by heating any accreted gas, keeping the galaxy red (e.g. Binney 2001; Ostriker & Ciotti 2005; Croton et al. 2006; Bower et al. 2006; Best et al. 2006; Cattaneo et al. 2007). While this proposed scenario is attractive in that it solves many outstanding questions relating to the formation of elliptical galaxies, it has yet to be confirmed observationally. Understanding what quenches star formation is critical to understanding how the red sequence is built up over time.

Post-starburst galaxies are potentially an ideal population with which to study the processes that quench star formation. Post-starburst galaxies are passing through a brief phase of galaxy evolution: they are seen just after abruptly ceasing star formation. These galaxies are also known as "E+A" or "K+A" galaxies from their spectral types, which show a mixture of older stars plus younger A stars (e.g. Dressler & Gunn 1983; Zabludoff et al. 1996; Quintero et al. 2004). Their spectra show strong Balmer absorption from A stars but no nebular emission, which indicates that they are not currently forming stars. However, the presence of A stars, which have lifetimes $\lesssim 1$ Gyr, show that star formation has only recently stopped. As these galaxies age, the A stars will disappear and their spectra will look like that of an early-type galaxy. Their morphologies and metallicities also imply that they are the immediate progenitors of early-type, red, spheroidal galaxies (Yang et al. 2008; Goto 2007). Post-starburst galaxies are therefore likely caught in the act of moving from the blue cloud to the red sequence.

[1] Department of Physics, Center for Astrophysics and Space Sciences, University of California at San Diego, 9500 Gilman Dr., La Jolla, San Diego, CA 92093
[2] Alfred P. Sloan Foundation Fellow
[3] Steward Observatory, The University of Arizona, 933 N. Cherry Ave., Tucson, AZ 85721
[4] Theoretical Division, Los Alamos National Laboratory, Los Alamos, NM 87545
[5] Department of Physics and Cosmology, University of California at Irvine, 4129 Frederick Reines Hall, Irvine, CA 92697
[6] Hubble Fellow, Center for Galaxy Evolution fellow
[7] Center for Cosmology and Particle Physics, Department of Physics, New York University, 4 Washington Place, New York, NY 10003

Observationally, there are a variety of ways in which to find evidence for the star formation quenching mechanism in these galaxies. One method is to search for outflowing galactic winds using either blueshifted interstellar medium (ISM) absorption lines (see Veilleux et al. 2005 for a recent review) or emission lines (Rubin et al. 2011). Detecting winds through blueshifted absorption has the advantage of providing kinematic information on the wind speed along the line of sight. The AGN gas blowout picture discussed above recently gained support with the discovery by Tremonti et al. (2007) of extreme velocity outflows in very luminous post-starburst galaxies at $z \sim 0.6$ selected from the Sloan Digital Sky Survey (SDSS, York et al. 2000). These galaxies are extremely rare, have low space densities, and are bright, blue, and massive ($\geq 10^{11}\ M_{\odot}$). The outflowing winds are detected in blueshifted Mg II 2796, 2803 Å interstellar absorption lines in ten of the fourteen galaxies observed. The outflow velocities seen in these galaxies are $\sim 1000$ km s$^{-1}$ or more, which the authors interpret as galaxy-scale AGN winds launched at the epoch of cessation of the starburst. The motivation for AGN activity as the driver of these winds is the high velocity of the outflows; the velocities seen are intermediate between winds in local starburst galaxies and winds in broad absorption line quasars.

Galactic-scale outflows can also be driven by supernovae (SNe) resulting from high star formation rates. At low redshift, outflows of ∼-100 to -600 km s$^{-1}$ are observed in infrared-luminous galaxies (SFR $\gtrsim$ 20-50 $M_{\odot}$ yr$^{-1}$) in the Na I D 5890, 5896 Å doublet (Heckman et al. 2000; Rupke et al. 2005; Martin 2005). At $z = 1.4$, where much of the blue galaxy population is forming stars with high SFR, $\sim 20 - 100\ M_{\odot}$ yr$^{-1}$, Weiner et al. (2009) found outflowing galactic winds detected as blueshifted absorption in the Mg II 2796, 2803 Å doublet by stacking spectra of star-forming galaxies in the DEEP2 redshift survey, with typical velocities of ∼-300 km s$^{-1}$. Similar results were found by Rubin et al. (2010) in star-forming galaxies at $z \sim 1$. At an even higher redshift of $z \sim 2 - 3$, Lyman-break galaxies also exhibit strong winds with speeds of ∼-200 – -500 km s$^{-1}$ (Shapley et al. 2003; Steidel et al. 2010).

The winds seen in these galaxies are likely SNe-driven, as opposed to AGN-driven, as most of these galaxies do not have detected AGN, and the fraction of star-forming galaxies with winds is high ($\gtrsim$ 50%). These SNe-driven winds raise the questions of whether AGN-driven outflows are necessary and/or sufficient to cause the quenching of star formation. High-luminosity AGN are expected to drive faster winds than star-formation powered objects (Thacker et al. 2006) and may be more effective at clearing the ISM of the host galaxy. The wind velocity can therefore potentially distinguish the cause of the galactic wind: starburst or AGN.

In the Thacker et al. (2006) model, which assumes that AGN drive outflows with an energy output equal to 5% of the bolometric luminosity, typical outflow velocities are ∼1000 km s$^{-1}$ and depend on the bulge (and therefore AGN) mass. For example, galaxies with bulge masses $> 10^{12}\ M_{\odot}$ (with corresponding AGN masses $> 10^{9}\ M_{\odot}$) drive outflows with velocities >1000 km s$^{-1}$, while galaxies with bulge masses $> 3\ 10^{11}\ M_{\odot}$ have typical velocities of 1000 km s$^{-1}$ but can have velocities of $\sim$ 700-800 km s$^{-1}$. They further show that winds in excess of 1000 km s$^{-1}$ are difficult to produce with SNe-driven winds and would require extremely efficient star formation, with a ratio of gas to stars of <25%. It is worth noting that the ∼1000 km s$^{-1}$ winds predicted in this model are for luminous AGN.

The Tremonti et al. (2007) sample included only a very specific and rare type of galaxy with low space density; it is not clear whether most red galaxies have followed this path to the red sequence. Their result therefore may not be applicable to the bulk of the red sequence. In this paper we present Keck/LRIS-B restframe UV spectra of a sample of ten X-ray selected narrow-line AGN host galaxies from the AEGIS survey and thirteen post-starburst galaxies at intermediate redshifts ($0.2 < z < 0.8$) from the SDSS and DEEP2 surveys. We observe galaxies with lower-luminosity AGN, both in star-forming and quiescent galaxies, as well as more common post-starburst galaxies, in order to measure the frequency and velocity of outflowing winds via blueshifted absorption in several UV ISM lines (Fe II 2343, 2374, 2382, 2586, 2599 Å, Mg II 2796, 2803 Å, and Mg I 2852 Å). Our aim is to determine (1) whether winds are frequently found in galaxies that host low-level (non-quasar) AGN, (2) whether winds are commonly associated with the truncation of star formation at intermediate redshift, (3) whether wind presence correlates with star formation activity, (4) whether the velocities indicate a star formation- or AGN-driven wind, and (5) whether the velocities are high enough to potentially clear the ISM of the galaxy and halt star formation. The galaxies in our study should represent typical paths to the red sequence; therefore our results are potentially relevant for the formation of much of the quiescent population.

Until very recently, the Fe II, Mg II, and Mg I lines have been little studied due to their location in the near-UV. Most $z < 1$ searches for absorption have used the Na I D doublet, however it is harder to interpret as (1) the velocity separation is low (304 km s$^{-1}$, as compared to the 770 km s$^{-1}$ separation of Mg II) such that it is often blended, (2) it has a lower ionization potential (5.1 eV for Na I D, compared to 15.0 eV for Mg II) and therefore traces dense gas while Mg II more faithfully traces cool, photoionized gas, and (3) the stellar contribution to Na I D is quite significant ( 80% in Chen et al.) and requires extensive modeling to separate the outflow and stellar components (e.g. Rupke et al. 2005; Chen et al. 2010). We choose here to focus on the Fe II, Mg II, and Mg I lines.

The outline of the paper is as follows: §2 describes our galaxy samples, LRIS spectra, and data reduction. In §3 we discuss the methods used in this paper to obtain absorption line fits to the UV lines of interest, including removing absorption due to stars or gas in the galaxy. We present results on winds detected in absorption in §4 and winds detected in emission in §5. We discuss our results and conclude in §6. In this paper all magnitudes are AB. Restframe magnitudes are $M - 5\ \log(h)$ with $h = 1$.

TABLE 1
PROPERTIES OF GALAXIES IN SAMPLE

| Object | RA (J2000) | Dec (J2000) | redshift | $B$ | $R$ | $I$ | $U-B$ | $M_B$ |
|---|---|---|---|---|---|---|---|---|
| X-ray AGN Host Galaxies | | | | | | | | |
| 11046507 | 14:16:04.970 | +52:18:27.971 | 0.4514 | 21.3 | 20.6 | 20.5 | 0.31 | -20.12 |
| 12016790 | 14:17:32.498 | +52:34:41.209 | 0.4645 | 20.9 | 19.9 | 19.6 | 0.56 | -20.91 |
| 13004312 | 14:19:10.463 | +52:48:31.240 | 0.3458 | 21.4 | 19.0 | 18.3 | 1.27 | -20.73 |
| 13025528 | 14:20:38.780 | +52:57:27.729 | 0.2004 | 19.9 | 18.1 | 17.6 | 1.10 | -20.12 |
| 13041622 | 14:21:12.279 | +53:06:22.173 | 0.2017 | 20.0 | 18.7 | 18.2 | 0.77 | -19.77 |
| 13043681 | 14:20:00.785 | +53:06:43.926 | 0.2014 | 20.0 | 18.0 | 17.4 | 1.25 | -20.20 |
| 13051909 | 14:19:49.857 | +53:08:05.335 | 0.2334 | 20.3 | 18.4 | 17.8 | 1.11 | -20.27 |
| 13063597 | 14:22:17.219 | +53:14:27.123 | 0.3029 | 19.9 | 18.4 | 17.8 | 0.84 | -21.15 |
| 13063920 | 14:21:41.788 | +53:15:06.358 | 0.5589 | 21.7 | 20.7 | 20.3 | 0.59 | -20.65 |
| 22029058 | 16:51:10.627 | +34:54:53.390 | 0.3407 | 20.3 | 19.3 | 18.9 | 0.49 | -20.61 |
| DEEP2 K+A Galaxies | | | | | | | | |
| 31046744 | 23:27:12.737 | +00:17:16.822 | 0.8542 | 23.9 | 22.4 | 21.2 | 1.03 | -20.99 |
| 32003698 | 23:30:14.824 | +00:01:29.920 | 0.7960 | 23.8 | 21.3 | 20.1 | 1.10 | -21.82 |
| 32008909 | 23:30:29.216 | +00:03:54.400 | 0.7894 | 24.2 | 22.1 | 21.1 | 1.01 | -20.85 |
| 41057700 | 02:27:28.413 | +00:48:04.204 | 0.7200 | 22.9 | 21.5 | 20.8 | 0.76 | -20.85 |
| 42020386 | 02:31:02.398 | +00:33:12.964 | 0.7757 | 23.1 | 21.6 | 20.8 | 0.81 | -21.10 |
| 42021012 | 02:30:54.429 | +00:32:50.010 | 0.7482 | 22.7 | 21.6 | 21.0 | 0.60 | -20.82 |
| 43030800 | 02:32:03.446 | +00:39:47.795 | 0.8445 | 23.7 | 22.8 | 21.7 | 1.02 | -20.50 |

| Object | RA (J2000) | Dec (J2000) | redshift | $u$ | $g$ | $r$ | $i$ | $z$ | $U-B$ | $M_B$ |
|---|---|---|---|---|---|---|---|---|---|---|
| SDSS K+A Galaxies | | | | | | | | | | |
| J022743.21−001523.0 | 02:27:43.211 | -00:15:23.077 | 0.2191 | 19.0 | 17.7 | 17.0 | 16.7 | 16.5 | 0.91 | -21.92 |
| J210025.41+011319.2 | 21:00:25.415 | +01:13:19.267 | 0.2079 | 20.5 | 18.9 | 17.9 | 17.6 | 17.4 | 1.13 | -21.00 |
| J212043.73+114345.4 | 21:20:32.739 | +11:43:45.430 | 0.2435 | 20.4 | 18.6 | 17.6 | 17.2 | 17.0 | 1.25 | -21.80 |
| J215518.35−071010.6 | 21:55:18.354 | -07:10:10.697 | 0.2767 | 21.0 | 19.0 | 17.8 | 17.4 | 17.2 | 1.14 | -21.62 |
| J224603.64−000918.8 | 22:46:03.640 | -00:09:18.804 | 0.2052 | 20.1 | 18.4 | 17.3 | 17.0 | 16.7 | 1.13 | -21.51 |
| J225656.77+130402.6 | 22:56:56.770 | +13:04:02.609 | 0.2089 | 19.8 | 18.1 | 17.3 | 17.0 | 16.7 | 1.10 | -21.61 |

TABLE 2
PROPERTIES OF X-RAY AGN HOST GALAXIES

| Object | log SFR[1] ($M_\odot\ yr^{-1}$) | log stellar mass ($M_\odot$) | log $L_X$ est. from SF ($erg\ s^{-1}$) | log $L_X$ from $f_{(0.5-2keV)}$ ($erg\ s^{-1}$) | log $L_X$ from $f_{(2-10keV)}$ ($erg\ s^{-1}$) | HR |
|---|---|---|---|---|---|---|
| DEEP2 X-ray AGN Host Galaxies | | | | | | |
| 11046507 | 1.10 | 9.82 | 40.50 | $41.60^{+0.21}_{-0.24}$ | $< 42.15$ | $-0.74^{+0.06}_{-0.26}$ |
| 12016790 | 1.41 | 10.97 | 41.02 | $41.93^{+0.16}_{-0.18}$ | $< 42.44$ | $-0.59^{+0.11}_{-0.41}$ |
| 13004312 | ... | 11.15 | 40.10 | $41.41^{+0.19}_{-0.21}$ | $< 41.83$ | $-0.68^{+0.08}_{-0.32}$ |
| 13025528 | 0.40 | 11.10 | 40.55 | $40.69^{+0.25}_{-0.30}$ | $41.63^{+0.18}_{-0.21}$ | $+0.26^{+0.31}_{-0.24}$ |
| 13041622 | 1.09 | 10.74 | 40.73 | $41.47^{+0.08}_{-0.08}$ | $41.66^{+0.18}_{-0.26}$ | $-0.48^{+0.20}_{-0.17}$ |
| 13043681 | ... | 10.52 | 39.47 | $41.39^{+0.11}_{-0.12}$ | $< 41.58$ | $-0.72^{+0.10}_{-0.25}$ |
| 13051909 | 1.08 | 11.40 | 41.01 | $42.11^{+0.08}_{-0.08}$ | $43.55^{+0.03}_{-0.03}$ | $+0.71^{+0.05}_{-0.04}$ |
| 13063597 | 1.21 | 10.53 | 40.75 | $41.50^{+0.19}_{-0.23}$ | $< 42.13$ | $-0.24^{+0.35}_{-0.34}$ |
| 13063920 | 1.62 | 11.18 | 41.23 | $41.79^{+0.26}_{-0.29}$ | $< 42.38$ | $-0.66^{+0.08}_{-0.34}$ |

[a]The columns list the star formation rate derived from MIPS 24$\mu$m flux, the stellar mass derived following Lin et al. (2007), the X-ray luminosity estimated from star formation alone, the X-ray luminosity at 2-10 keV derived from the observed X-ray flux at either 0.5-2 keV or 2-10 keV, and the hardness ratio (see text for details).

## 2. DATA

### 2.1. *Galaxy Samples*

For this study we selected two samples of intermediate redshift galaxies to study their outflowing wind properties: 1) X-ray AGN host galaxies, and 2) post-starburst ("K+A") galaxies. Properties of the galaxies in our samples are given in Table 1. The redshifts listed are derived from our LRIS data. K-corrections, absolute $M_B$ magnitudes and restframe $(U-B)$ colors for DEEP2 objects have been derived as described in Willmer et al. (2006) and for SDSS objects were derived using the kcorrect package (Blanton & Roweis 2007). We do not include luminosity evolution in the K-corrections for $M_B$.

X-ray AGN host galaxies were identified using deep 200 ks *Chandra* data (Laird et al. 2009) obtained as part of the AEGIS survey (Davis et al. 2007). The *Chandra* data reduction, source detection and flux estimation are described in detail by Laird et al. (2009). Initial optical spectroscopy of these sources was provided by the DEEP2 survey (Davis et al. 2000, 2003) using DEIMOS on Keck and by Coil et al. (2009) using Hectospec on the MMT. Here we present follow-up LRIS-B spectroscopy of nine X-ray AGN host galaxies with redshifts $0.20 < z < 0.56$ and $B < 21.7$. We selected sources that are bright in the $B$ band, such that we would be able to detect continuum levels in their spectra with relatively short exposures (under an hour), and we did not target objects with broad Mg II emission in their DEEP2 or MMT spectra, as strong broad emission may have affected our ability to detect blueshifted absorption features.

Table 1 lists additional properties of these X-ray sources. Shown are the SFRs derived from MIPS 24$\mu$m observations of the AEGIS field (Davis et al. 2007), following the prescription of Rieke et al. (2009). These SFR estimates are upper limits as there may be some contribution to the IR luminosity from an AGN. All but one of the sources are detected in the MIPS data; for the non-detection the SFR should be extremely low. We list stellar masses derived following the prescription of Lin et al. (2007) for DEEP2 galaxies. Using the stellar mass and SFR, we estimate the X-ray luminosity expected from X-ray binaries, following Lehmer et al. (2010). We list the X-ray luminosity (at 2-10 keV restframe) that is estimated from the observed *Chandra* flux in either the soft or hard bands, assuming $\Gamma$ =1.9, corrected for Galactic absorption but assuming no intrinsic absorption. If the source was not detected in the hard band, an upper limit is given based on the 99% upper limit on the observed flux. We also list the hardness ratio, estimated using Bayesian techniques as described in Laird et al. (2009), following Park et al. (2006). Two of our nine X-ray sources have positive hardness ratios, indicative of moderately obscured AGN. One of those also has log $L_{\rm X} > 42$ erg s$^{-1}$, above the traditional cutoff often used to define AGN. The other seven sources have log $L_{\rm X} \sim 41-42$ erg s$^{-1}$. The log $L_{\rm X}$ values estimated from the observed X-ray fluxes are typically $\sim$10 times higher than the upper limits on the contribution to log $L_{\rm X}$ estimated from their SFRs. We therefore conclude that these galaxies have low luminosity, relatively unobscured AGN. We note that while these are relatively low luminosity AGN, they should be fairly representative of the broader population of low luminosity AGN at these redshifts.

During our observations of the X-ray AGN host galaxies we also observed one luminous infrared galaxy (LIRG) in the DEEP2 16hr field that was selected as a *Spitzer*/MIPS 24 $\mu$m source with high $L_{IR}$. The DEEP2 16hr field was observed with MIPS by the MIPS GTO team in August 2007. The observations were reduced with the MIPS GTO pipeline and fluxes cataloged using DAOphot PSF fitting. For 24 $\mu$m sources without DEEP2 redshifts, follow-up spectra were obtained with MMT/Hectospec. A full catalog will be published in a forthcoming paper. We computed the total IR luminosity from the 24 $\mu$m flux, K-correcting with a template from Dale & Helou (2002). This source has a total IR luminosity of log $L_{IR} > 11.7$ $L_\odot$. We selected a source at intermediate redshift ($z = 0.34$) that was bright at observed blue wavelengths ($B = 20.3$) and did not have broad optical emission lines. It is not detected in relatively shallow *XMM* and *Chandra* data of this field and has an upper limit of log $L_{\rm X} < 44$ erg s$^{-1}$. While we do not know if this source contains an AGN, we include it in our 'X-ray AGN host galaxy' sample for the purposes of this paper, as it was selected to be IR-bright (and is not a post-starburst galaxy).

Post-starburst (K+A) galaxies were identified in both the DEEP2 and SDSS surveys from the optical spectroscopy. We decomposed spectra in each survey into two components: a young and an old stellar population. The templates were constructed using Bruzual & Charlot (2003) models with a Salpeter IMF and solar metallicity. The young population template is a model taken 0.3 Gyr after a starburst, which had a constant star formation rate and a duration of 0.1 Gyr. The old stellar population template is a 7 Gyr old simple stellar population. Using a linear decomposition, we measure the fractional contribution of the young component between 4450–4550 Å in the restframe, denoted as the A-star fraction ($f_A$). Post-starburst galaxies were identified as having a strong young stellar component ($f_A > 0.25$) and a weak or non-detectable H$\beta$ emission equivalent width (EW; Eq. 2 in Yan et al. 2009). We restricted the SDSS sample to $z > 0.2$ so that the observed Mg II 2796, 2803 Å doublet falls redward of 3360 Å, for better sensitivity. In the DEEP2 sample we can only identify post-starbursts to $z = 0.9$, where the spectral coverage includes the Balmer lines. We observed a total of seven K+A galaxies in DEEP2 with redshifts $0.77 < z < 0.85$ and $B < 24.2$ and six K+A galaxies in SDSS with redshifts $0.21 < z < 0.28$ and $u < 21$.

Restframe color-magnitude diagrams for the DEEP2 ($0.2 < z < 1.2$) and SDSS main galaxy ($0.02 < z < 0.20$) samples are shown in Figure 1, with our targets marked. Our sample of X-ray AGN host galaxies (shown as blue squares in the left panel of Figure 1) spans both the blue cloud and red sequence. We purposely targeted both blue and red host galaxies in order to study the prevalence of winds in both AGN host populations. Visual inspection of HST/ACS imaging of AEGIS AGN host galaxies in the blue cloud shows that the blue light in these objects is galaxy light and not dominated by a central blue point source; therefore our AGN host sample includes both star-forming and quiescent galaxies.

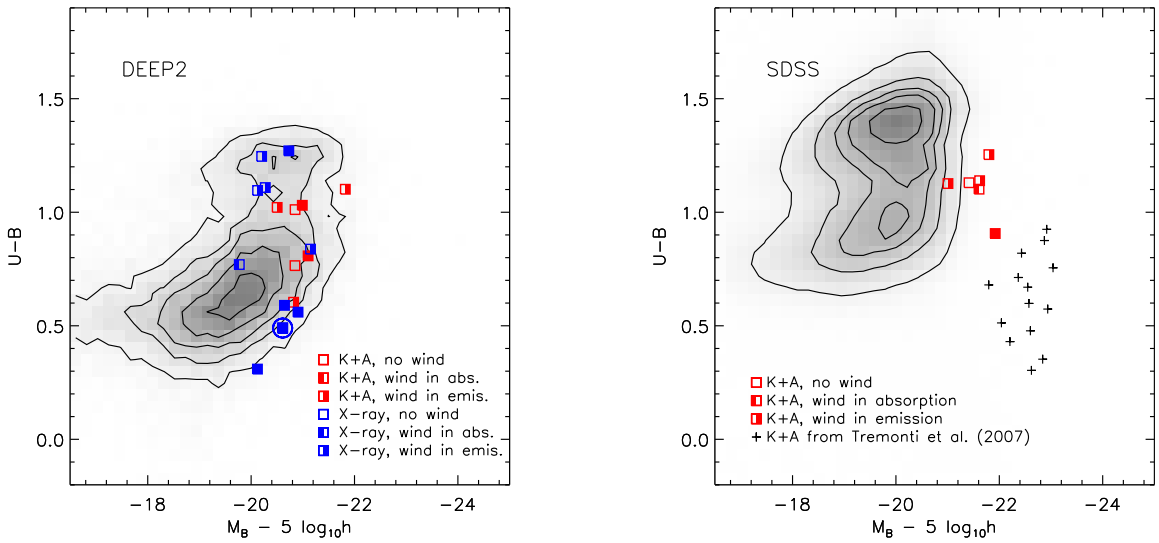


FIG. 1.— Left: Restframe $U-B$ color versus $M_B$ magnitude of galaxies in the DEEP2 parent galaxy sample with $0.2 < z < 1.2$ (grey shaded contours) compared to galaxies in our DEEP2 K+A sample (red squares) and AEGIS X-ray AGN host galaxies (blue squares). Filled red and blue squares are those galaxies in our sample with winds detected either by blueshifted Mg II absorption (left side of square filled) or by Mg II or Fe II* emission (right side of square filled). Objects with winds detected both in absorption and emission are shown with completely filled squares. The LIRG is indicated with a blue circle. Right: Restframe color-magnitude diagram of galaxies in the SDSS main galaxy sample with $0.02 < z < 0.20$ (grey shaded contours) compared to galaxies in our SDSS K+A sample with $0.20 < z < 0.28$ (red squares). Symbols are filled according to how a wind is detected, as in the left panel. K+A galaxies from Tremonti et al. (2007) are shown as black crosses.

Galaxies in our DEEP2 K+A sample (shown as red squares in the left panel of Figure 1) lie either at the bright end of the blue cloud or in the "green valley" between the blue cloud and red sequence. This reflects the fact that these galaxies recently stopped forming stars and are in transition, moving towards the red sequence. Our SDSS K+A sample, with $0.20 < z < 0.28$, is compared in the right panel of Figure 1 to the main SDSS galaxy sample at lower redshifts, $0.02 < z < 0.20$. At $z \sim 0.2$ SDSS targeted only very bright galaxies, with $M_r^{0.1} < -21.2$. Therefore, compared to the main SDSS sample, our SDSS K+A sample is composed of brighter galaxies. All but one of the galaxies in our SDSS K+A sample lie in the green valley; the other K+A galaxy is in the blue cloud. For comparison, we also plot the K+A sample of Tremonti et al. (2007), which is at $0.5 < z < 0.7$, in the right panel. The Tremonti et al. (2007) sample is brighter and bluer than our lower redshift SDSS K+A galaxies. This likely indicates that most galaxies in our SDSS K+A sample are at a slightly later evolutionary stage than the galaxies in the Tremonti et al. (2007) sample.

### 2.2. *Observations*

Observations of both samples were performed with the Low Resolution Imaging Spectrograph (LRIS, Oke et al. 1995) on the Keck I 10m telescope. The high UV/blue throughput of LRIS opens up the possibility of observing restframe UV lines at intermediate redshift. The X-ray AGN host sample was observed on April 23, 2009 with clear skies and 1-1.5″ seeing. The details of the spectrograph setup are given in Table 3. All objects were observed with the 1.0″ longslit. When possible two objects were placed on the longslit, otherwise the slit position angle was set to parallactic. LRIS has an atmospheric dispersion corrector (ADC, Phillips et al. 2008), which was used. The blue side data were binned both spatially and spectrally. Total exposure times varied between 20 to 60 minutes per object. Standard stars were taken at the beginning and end of the night and flats were taken in twilight.

The post-starburst sample was observed August 28 and 29, 2008, with clear skies and ∼0.7-1.2″ seeing. The SDSS objects were observed with the 1.0″ longslit. Again, when possible two objects were placed on the longslit, otherwise the slit position angle was set to parallactic, and the ADC was used. Total exposure times varied between 30 to 60 minutes per object. The DEEP2 post-starburst galaxies were observed on slitmasks with 1″ slit widths. Total exposure times varied between 1 to 3 hours per slitmask. The blue side data were binned both spatially and spectrally. Standard stars were taken at the beginning and end of the night and flats were taken in twilight.

### 2.3. *Data Reduction*

The data were reduced using the XIDL LowRedux [1] data reduction pipeline. The pipeline includes bias subtraction and flat fielding, wavelength calibration, object identification, sky subtraction, cosmic ray rejection, and flux calibration.

The wavelength solutions (which are extremely important for measuring velocity shifts to detect outflowing winds, as we do here) were checked by eye both in terms of the scatter in the arc solution (the resulting rms is ∼0.8 Å in the blue and 0.1 Å in the red for the X-ray AGN host galaxies and ∼0.2 Å in the blue and 0.05 Å in the red for the post-starburst galaxies) and by checking the

[1] http://www.ucolick.org/~xavier/LowRedux/

TABLE 3
LRIS Observational Setup for Each Sample

| | X-ray AGN | DEEP2 K+A | SDSS K+A |
|---|---|---|---|
| grism (line mm$^{-1}$) | 400 | 600 | 1200 |
| dichroic | d560 | d560 | d460 |
| grating (line mm$^{-1}$) | 600 | 600 | 600 |
| red central wave. (Å) | 6800 | 6900 | 6200 |
| blue wave. range (Å) | ∼1900–5600 | ∼3300–5600 | ∼2900–3900 |
| blue dispersion (Å pix$^{-1}$) | ∼2.1 | ∼1.2 | ∼0.5 |
| blue FWHM (Å) | ∼6.8 | ∼4.3 | ∼1.7 |
| red wave. range (Å) | ∼5600–8200 | ∼5600-8200 | ∼4900-7500 |
| red dispersion (Å pix$^{-1}$) | ∼1.3 | ∼1.3 | ∼1.3 |
| red FWHM (Å) | ∼5.8 | ∼5.8 | ∼5.8 |

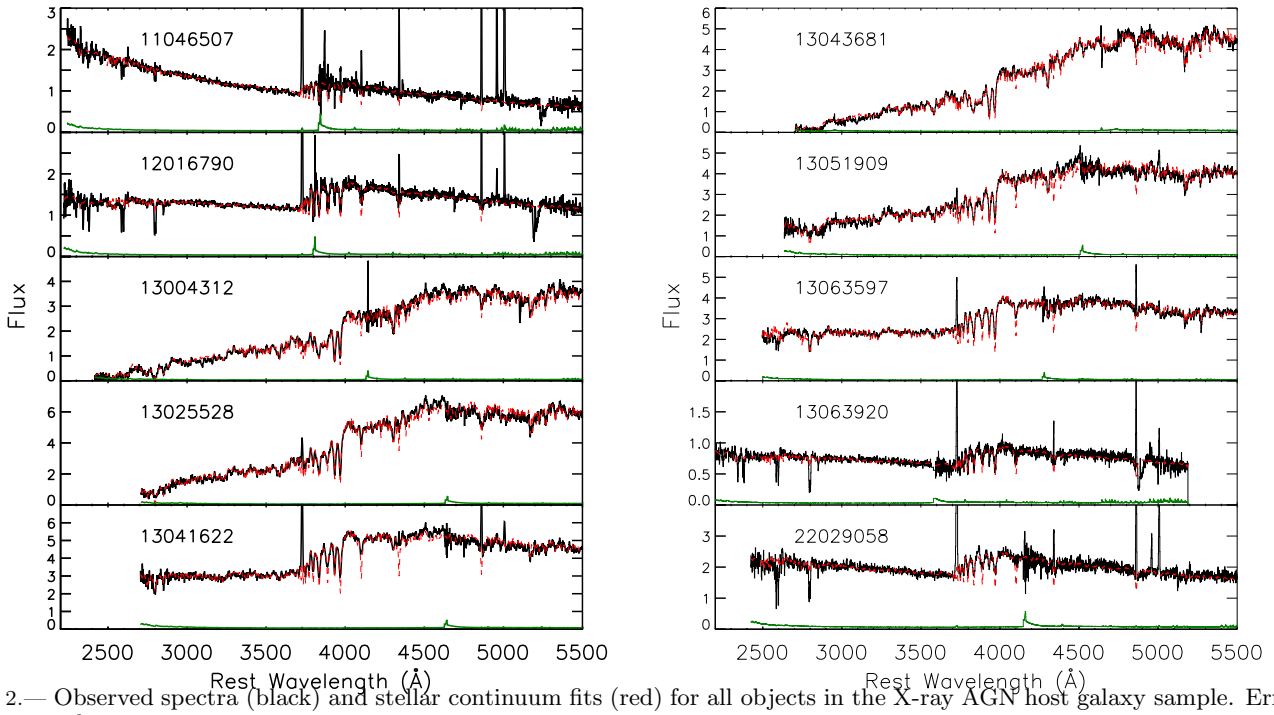


Fig. 2.— Observed spectra (black) and stellar continuum fits (red) for all objects in the X-ray AGN host galaxy sample. Error spectra are shown in green.

wavelengths of prominent sky lines across the observed wavelength range (at 3910 Å, 5577 Å, and 7341 Å). The final spectra are in air wavelengths. We flux calibrated our spectra using standard stars that were observed with the longslit using the same observational setup.

Redshifts for all of the sources were measured in the LRIS spectra using IDL code adapted from the DEEP2 data reduction pipeline. Using the redshift derived from the pre-existing DEIMOS or MMT spectra as an initial guess, we performed a $\chi^2$-minimization between the observed red-side LRIS data (to not be affected by the Fe II, Mg II, or Mg I absorption lines on the blue side) and a linear combination of three galaxy templates: an artificial emission-line galaxy spectrum, an early-type spectrum, and a post-starburst spectrum. The resulting best-fit redshifts were checked by eye and are used here to define the systemic velocity of each galaxy.

The typical redshift error from the $\chi^2$ fit is $<1e^{-5}$ and is therefore negligible. However, as any systemic shifts in the wavelength solutions between the blue and red side data would affect the e stimated systemic velocity, we also measure redshifts for the blue side data for the X-ray AGN objects with O II (3727 Å) emission and/or Balmer absorption lines and find that the redshift difference is typically $\sim$ 10 km s$^{-1}$. For the K+A objects the lines of interest all fall on the red side, so this test can not be performed.

## 3. ANALYSIS

The observed spectra are the product of a stellar population spectrum, ISM absorption occurring at the systemic velocity, and blueshifted absorption from outflowing gas, if it exists. To decompose these we first model the stellar population (sec 3.1) and then the systemic absorption (sec 3.2).

### 3.1. *Stellar Continuum Fits*

Older stellar populations can show significant stellar Mg II and Mg I absorption. While this absorption will

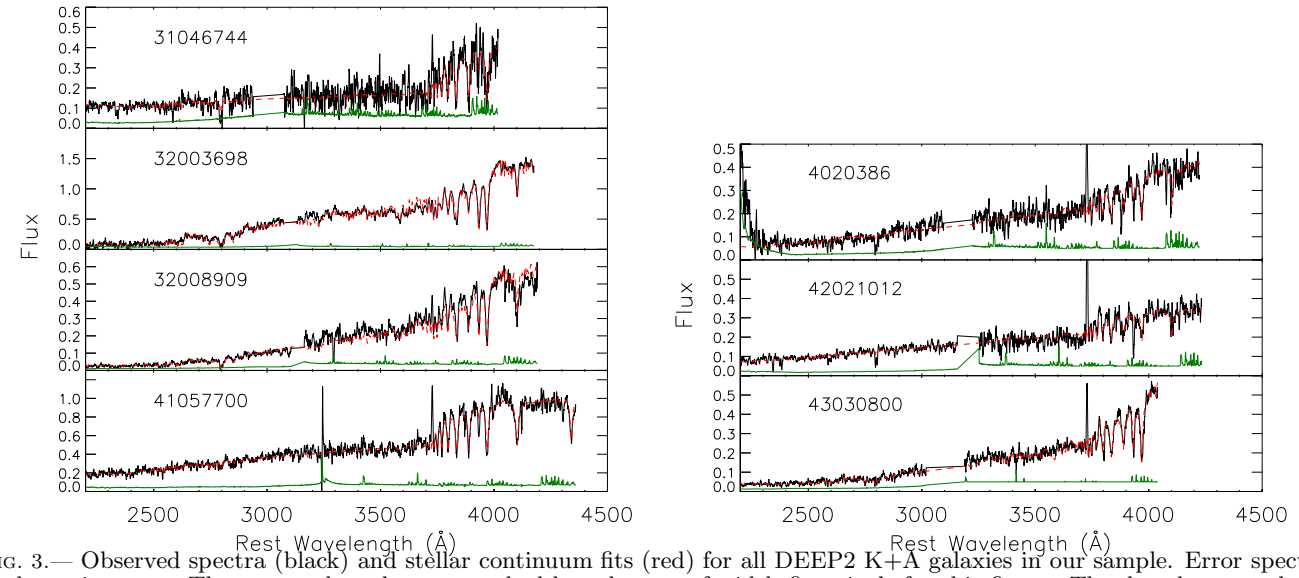


FIG. 3.— Observed spectra (black) and stellar continuum fits (red) for all DEEP2 K+A galaxies in our sample. Error spectra are shown in green. The spectra have been smoothed by a boxcar of width five pixels for this figure. The data have not been smoothed for any of the analysis presented.

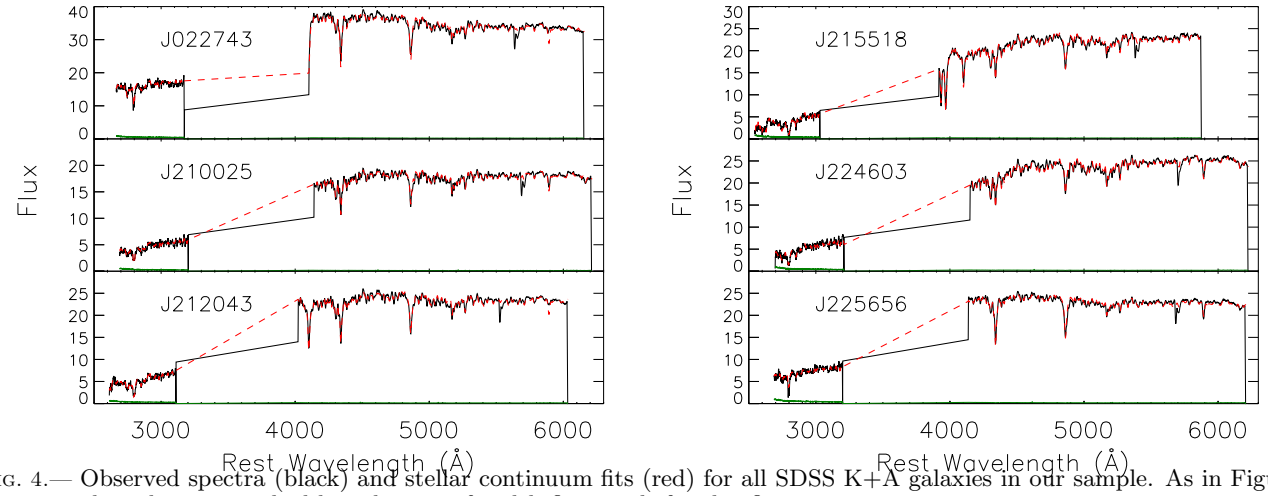


FIG. 4.— Observed spectra (black) and stellar continuum fits (red) for all SDSS K+A galaxies in our sample. As in Figure 3, the spectra have been smoothed by a boxcar of width five pixels for this figure.

likely not be relevant for our galaxies where the UV continuum is dominated by younger stars, it is potentially important for the red X-ray AGN host galaxies and the K+A galaxies in our sample. To estimate and account for stellar Mg II and Mg I absorption in our spectra, following Tremonti et al. (2007) we model the stellar continuum in our LRIS spectra by fitting each spectrum with a linear combination of Bruzual & Charlot (2003) single stellar population (SSP) models and adopt the model with the minimum $\chi^2$. A total of ten solar metallicity models are used, spanning a range of ages from 5 Myr to 10 Gyr, and reddening is treated as a free parameter. As discussed in Tremonti et al. (2007), the Bruzual & Charlot (2003) models use the Pickles (1998) stellar library which has a spectral resolution of 10 Å at wavelengths less than 3300 Å, which is too low to model the Mg II 2796, 2803 Å doublet at the resolution required. Therefore theoretical spectra from the UVBLUE stellar library (Rodríguez-Merino et al. 2005) are used for wavelengths 2600-3300 Å. While this does not include the wavelength range of the various Fe II lines studied here, in the best fit models to our data there is essentially no Fe II absorption. We are mainly interested in modeling the Mg II and Mg I stellar absorption. In deriving these fits we do not include the region of the spectra with rest wavelengths between 2760 Å and 2870 Å, to avoid the Mg II and Mg I absorption features in our data.

The fluxed spectra (black) and resulting stellar continuum fits (red) are shown for each sample in Figures 2-4. Close inspection of the Ca H+K and Balmer absorption features in the fits and data show that the fits reproduce the data well redward of 3900 Å and should therefore be reasonably good estimates of the stellar absorption at Mg II and Mg I.

The best-fit continuum model can be used to provide a rough estimate of the age of the stars in each galaxy. For the post-starburst sample in particular we are interested in the time since the last episode of star formation. For the X-ray AGN host galaxy sample, the ages estimated

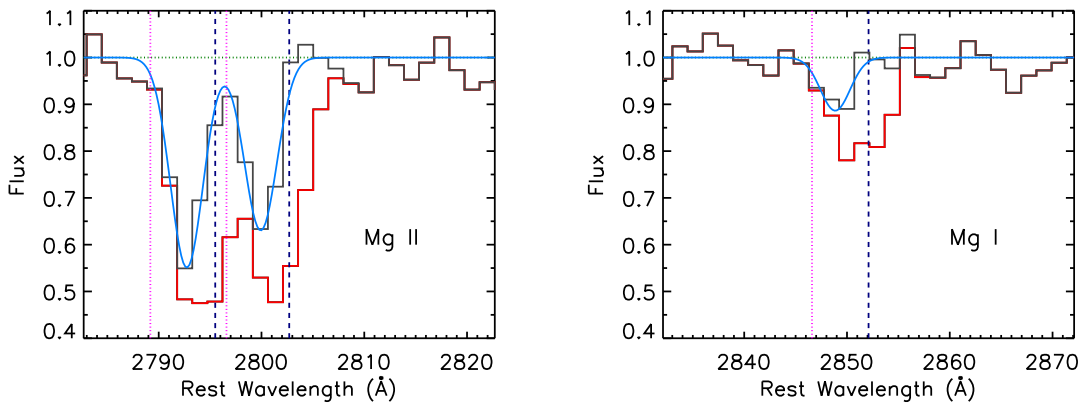


Fig. 5.— Absorption profiles for Mg II and Mg I for one of the X-ray AGN host galaxies, object 12016790. The red line is the observed continuum-normalized flux, the dark grey is the continuum-normalized flux after removing the systemic absorption, and the best-fit Gaussian to the grey data is shown in light blue. The continuum level is shown as a dotted green line, and the Mg II and Mg I lines at rest are shown as dashed dark blue lines, indicating the systemic velocity of each line. The maximum interval over which the equivalent width is measured is shown as a dotted pink line; this also corresponds to the maximum velocity that we report for each object with a wind observed in absorption.

TABLE 4
Light-Weighted Stellar Age Estimates

| Object | Light-Weighted Age (Gyr) | <2 Gyr Light Fraction | <2 Gyr Age (Myr) |
|---|---|---|---|
| X-ray AGN Host Galaxies | | | |
| 11046507 | 0.35 ±0.25 | 0.9 | 36 ±8 |
| 12016790 | 0.06 ±0.00 | 1.0 | 61 ±2 |
| 13004312 | 6.03 ±1.10 | 0.2 | 640 ±12 |
| 13025528 | 5.48 ±1.79 | 0.4 | 640 ±9 |
| 13041622 | 1.03 ±0.04 | 0.7 | 505 ±15 |
| 13043681 | 4.37 ±0.16 | 0.2 | 1,434 ±88 |
| 13051909 | 3.07 ±1.82 | 0.3 | 850 ±245 |
| 13063597 | 1.45 ±0.42 | 0.6 | 753 ±346 |
| 13063920 | 0.06 ±0.00 | 1.0 | 59 ±3 |
| 22029058 | 0.52 ±2.08 | 0.9 | 127 ±375 |
| DEEP2 K+A Galaxies | | | |
| 31046744 | 0.37 ±0.06 | 1.0 | 365 ±64 |
| 32003698 | 4.54 ±0.25 | 0.6 | 696 ±147 |
| 32008909 | 6.55 ±0.34 | 0.4 | 161 ±31 |
| 41057700 | 0.54 ±0.12 | 1.0 | 543 ±116 |
| 42020386 | 2.16 ±12.0 | 0.6 | 732 ±5940 |
| 42021012 | 0.49 ±0.07 | 1.0 | 488 ±65 |
| 43030800 | 0.59 ±0.06 | 1.0 | 592 ±56 |
| SDSS K+A Galaxies | | | |
| J022743 | 0.80 ±1.07 | 1.0 | 801 ±1074 |
| J210025 | 2.54 ±8.48 | 0.7 | 805 ±8483 |
| J212043 | 0.96 ±1.23 | 1.0 | 957 ±1225 |
| J215518 | 2.17 ±0.75 | 0.7 | 813 ±754 |
| J224603 | 1.89 ±12.0 | 0.3 | 686 ±12.0 |
| J225656 | 0.78 ±0.20 | 1.0 | 781 ±198 |

from these fits are generally secure, as the LRIS spectra taken for this study cover red enough wavelengths to constrain the older stars and cover the Balmer absorption lines. For the DEEP2 K+A sample, our LRIS spectra do not extend redward of ∼4000 Å, and so are not sensitive to older stellar populations. We therefore fit the DEEP2/DEIMOS spectra of these sources to estimate the light-weighted age. The ages derived from the DEIMOS and LRIS spectra for this sample are similar, such that the stellar continuum fit used to normalize the spectra is similar. For the SDSS K+A sample, our LRIS spectra extend to red wavelengths but do not cover the spectra region that contains Balmer absorption features. We therefore fit the SDSS spectra to estimate the ages of these galaxies.

Table 4 lists the light-weighted mean of the ages of the SSPs in the best-fit model for each object in our sample, where we include a rough estimate of the light-weighted age, the fraction of the light that is due to relatively young (<2 Gyr) stars, and the light-weighted age of the young (<2 Gyr) stars only. We note that there is an error of at least 1 Gyr on the light-weighted age of the stars and an error of at least 200 Myr on the age of the young population due to fitting degeneracies. We use these age estimates merely to establish relative ages between galaxies in our sample. Comparing the DEEP2 and SDSS K+A samples, we find that stars in the younger stellar population of the SDSS K+A galaxies is older, on average, which may not be surprising given that the SDSS galaxies are at lower redshift.

We use the stellar continuum fits to correct any small residual fluxing errors in our data below rest wavelengths 2900 Å, by ensuring that the ratio of the fit to the continuum level in our spectra is close to unity in regions around the Fe II, Mg II, and Mg I lines of interest. We then divide the data by the fit to produce continuum-normalized spectra where the continuum fit includes the stellar absorption, so that the normalized spectra show the excess or non-stellar absorption.

Errors on the stellar continuum model will propagate to the continuum-normalized spectra. This may be particularly important for Mg II, as there is substantial Mg II absorption in older stellar populations. We estimate the error on the Mg II stellar absorption EW by creating 25 Monte Carlo realizations of continuum spectra, drawn from the error distributions of the individual SSP fit amplitudes. For the X-ray AGN host galaxies, the median Mg II EW error is 3% and therefore negligible. There is one galaxy, 13051909, for which the error is

20%; the relevance of this is discussed further in Section 5.1.

For the DEEP2 K+A galaxies, the median stellar continuum Mg II EW error is 9% and is subdominant. There are two objects that have larger Mg II EW errors: 42020386 (32%) and 43030800 (26%); these are discussed further in Sections 4.1 and 5.1. For the SDSS K+A galaxies, the continuum errors are negligible ($< 2\%$) using the best fits to the LRIS spectra. However, for the DEEP2 and SDSS K+A galaxies, there may be additional systematic errors in the stellar continuum, as the LRIS spectra do not include red wavelengths for the DEEP2 sources or the Balmer series for the SDSS sources. We may therefore be underestimating the Mg II photospheric absorption in the DEEP2 stellar continua and overestimating the Mg II photospheric absorption in the SDSS stellar continua. This would imply that the SDSS wind absorption EWs that we measure are a conservative lower limit; however, the DEEP2 wind absorption EWs may be overestimated. The importance of this can be determined by comparing the Mg II EW in the LRIS stellar continuum best-fit models and those from the DEIMOS and SDSS spectra. The EWs are generally similar between the LRIS and DEIMOS/SDSS spectra and therefore our measurements should not be significantly affected. This is discussed further in Section 5.1 below.

In addition, we produce separate continuum normalized spectra that that are normalized by a smooth continuum not including stellar absorption. These spectra are used to estimate how much our results are biased if stellar absorption is *not* explicitly accounted for. To create these spectra we use the best fit model above to define the broad shape of the continuum level. We divide the model fit into bins ∼50 Å wide and use the maximum value of the fit in that bin as an estimate of the continuum level. This ensures that we use the continuum level of the fit but do not include any absorption lines. The width of 50 Å is large enough to ensure that no absorption line features contribute but is small enough to retain the shape and wiggles in the overall continuum level. We then interpolate this coarse continuum estimate onto the wavelength grid in the data, and divide the observed spectrum by the continuum estimate. Investigating the continuum-normalized spectra by eye, we conclude that this method works well for our purposes.

### 3.2. *Absorption Line Fits*

We model the Fe II, Mg II, and Mg I absorption lines in our data by fitting a Gaussian to the continuum-normalized spectra, from which we can estimate the velocity offset of the center of the absorption profile, the velocity width of the profile, and the lower limit on the covering fraction (equal to the observed absorption depth).

First, following Weiner et al. (2009) we attempt to separate absorption due to outflowing gas from absorption due to the ISM of the galaxy (i.e. not in an outflow component) with the following model:

$$F_{obs}(\lambda) = C(\lambda)(1 - A_{sym})(1 - A_{flow}), \qquad (1)$$

where $F_{obs}(\lambda)$ is the observed flux density, $C(\lambda)$ is the underlying stellar continuum fit, and $A_{sym}$ and $A_{flow}$ are the absorption features from the intrinsic (symmetric) and outflow (blueshifted) absorption. To estimate the intrinsic ISM absorption of the galaxy, if any, we first fit a Gaussian to the continuum-normalized flux and use the result to model the absorption *redward* of the systemic velocity for each line as an estimate of the systemic absorption. We assume that this absorption is symmetric about the systemic velocity of the line and divide out this model fit to the data both blueward and redward of the systemic velocity. We then fit the resulting data (where the remaining absorption should be due only to an outflowing component) with a new Gaussian. This step of removing the systemic absorption is performed only for those objects and lines in which the data redward of the systemic velocity was negative (i.e. showed absorption). Only galaxies in the blue cloud show this absorption, including four X-ray AGN host galaxies, two DEEP2 K+A galaxies, and one SDSS K+A galaxy, not all of which have detected blueshifted absorption.

For the Mg II 2796, 2803 Å and Fe II 2586, 2599 Å lines we model the symmetric absorption as the product of two Gaussians $G(v)$ centered on the wavelengths $\lambda_1, \lambda_2$, with velocity dispersion $\sigma$ and intensities $A_1, A_2$:

$$A_{sym}(\lambda) = A_1 G(v, \lambda_1, \sigma) + A_2 G(v, \lambda_2, \sigma) \qquad (2)$$

For the Fe II 2586, 2599 Å lines we allow $A_1$ and $A_2$ to be fit independently.

For the Mg II 2796, 2803 Å doublet the systemic component of the bluer line may be impacted by absorption from the outflowing wind component of the redder line. We therefore use the measured systemic component from the redder line alone for both lines in the doublet, assuming that the systemic component is the same for both, which would be true if the systemic absorption in the Mg II line is saturated. Given that the ratio of the minimum absorption in the two lines is close to unity, this assumption of $\tau > 1$ is well justified. We then remove this systemic absorption from both lines in the doublet and fit the remaining data with a double Gaussian, where we restrict both lines to have the same velocity width but allow the relative depths of the lines to vary.

The Gaussian fit to the remaining absorption blueward of systemic provides an estimate of the velocity centroid of the outflowing wind, the velocity width of the wind, and the minimum line depth. The covering fraction is simply 1 - the minimum line depth (or $A_{flow}$) if the data are high resolution and the line is optically thick; here we can only obtain a lower limit on the covering fraction due to our resolution.

As the various AGN and K+A samples were observed using different blue side grisms, the velocity resolution varies. The resolution at 2800 Å restframe for the X-ray AGN sample is ∼540 km s$^{-1}$, while for the DEEP2 K+A sample it is ∼250 km s$^{-1}$, and for the SDSS K+A sample it is ∼150 km s$^{-1}$. These differences will affect measurements of the velocity width and line depth, which should be interpreted with caution. However, they should not significantly affect the velocity centroid or our ability to detect outflows, which is dominated by the S/N of the spectra. As discussed above, only a few galaxies in our sample with blueshifted absorption have systemic absorption removed. While in theory this, when combined with the different velocity resolution of our sam-

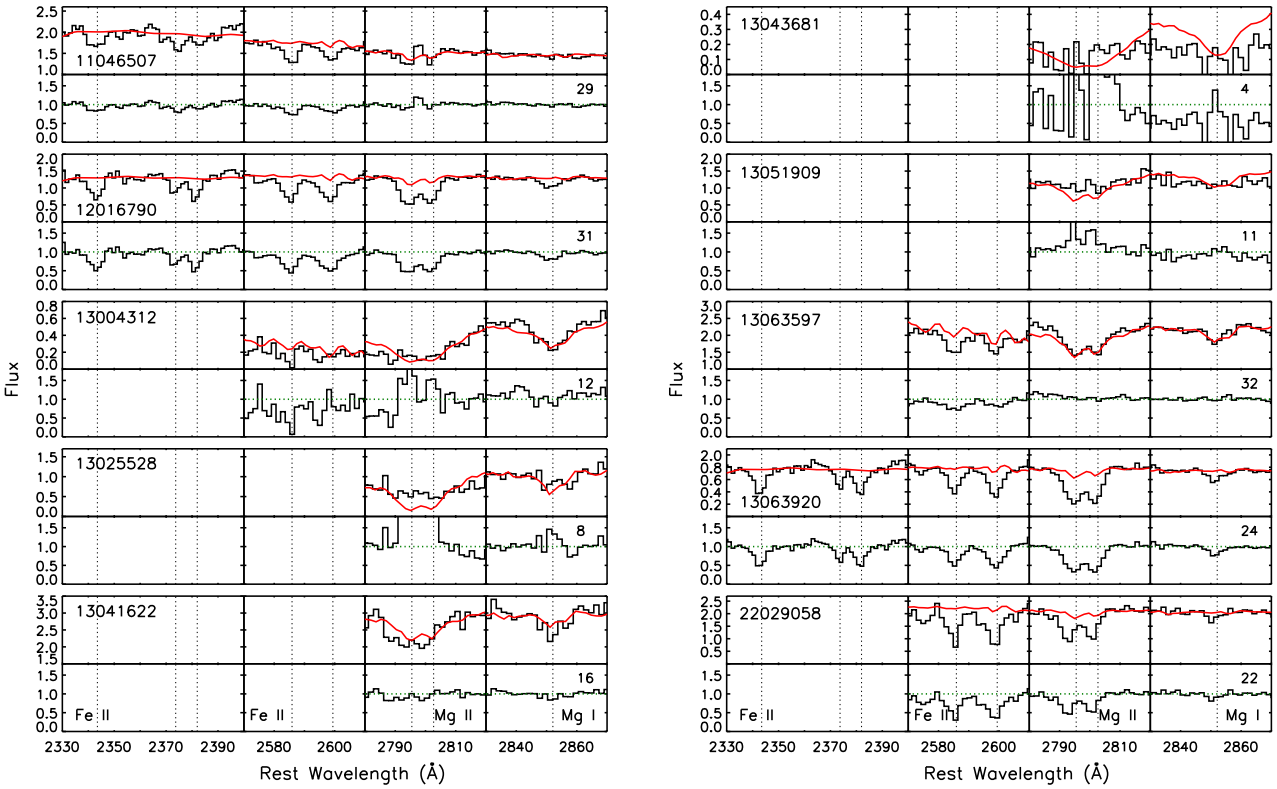


FIG. 6.— Regions of the observed and continuum-normalized spectra around Fe II, Mg II, and Mg I for objects in the DEEP2 X-ray AGN host galaxy sample. For each object we plot two rows of spectra; the top row shows the observed spectrum (black) and stellar continuum fit (red), while the bottom row shows the continuum-normalized spectrum (black) and continuum level (green). We do not show spectra with the systemic component removed. In the lower right panel for each galaxy we list the median S/N/pixel averaged between two windows near Mg II and Mg I: 2650–2750 Å and 2900–3000 Å.

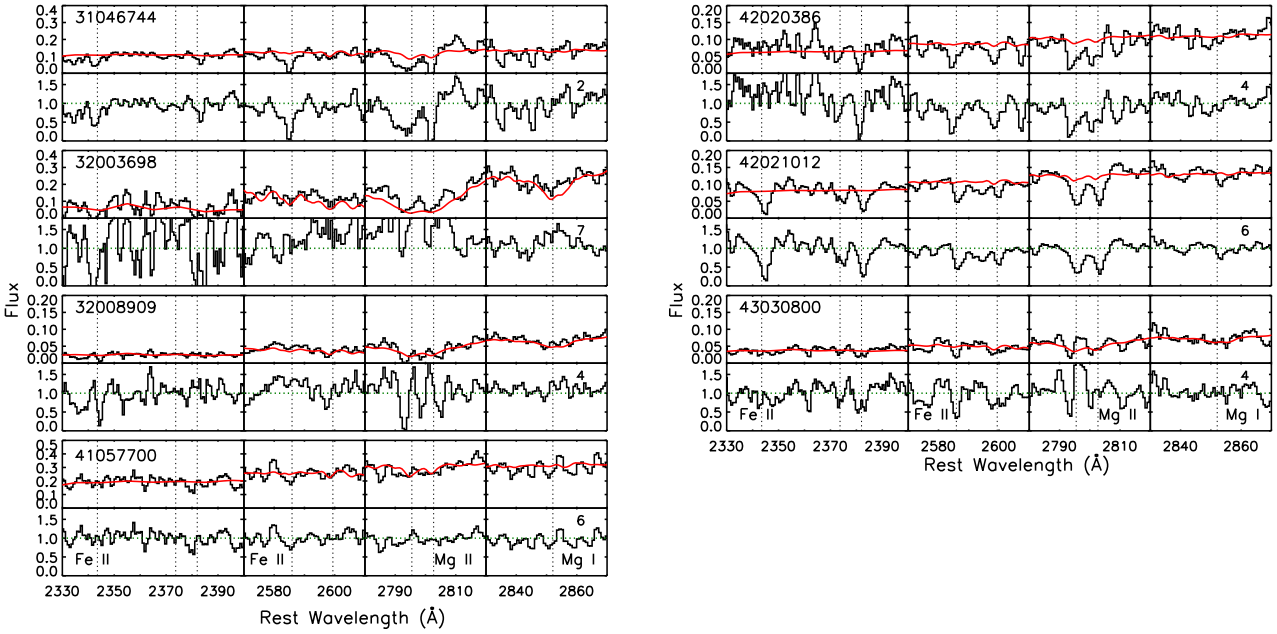


FIG. 7.— Regions of the observed and continuum-normalized spectra around Fe II, Mg II, and Mg I for objects in the DEEP2 K+A galaxy sample, similar to Figure 6.

ples, could affect the velocity centroid of the outflow in these objects, in one X-ray AGN host galaxy where systemic absorption is removed from the Fe II lines but not the Mg II doublet (due to the presence of Mg II emission), the outflow velocity centroids of the Fe II and Mg II lines are consistent with each other.

From the Gaussian fit we can estimate where the blueward flux of the fit is within $1\sigma$ of the continuum; we call this the 'maximum velocity' of the wind. We integrate the continuum-normalized flux from the systemic velocity to this maximum velocity to measure the EW and associated error. The velocity range used to measure the EW therefore varies from object to object. This approach is summarized in Figure 5, which shows the results of fitting the Mg II doublet and Mg I for an X-ray AGN host galaxy.

The absorption EW is measured after removing any systemic component, such that it is the EW of the outflow component alone. Without subtracting systemic absorption due to ISM in the galaxy, any estimates of the outflow kinematics or EW may be systematically biased. For example, for the Mg I line shown in Figure 5, the EW is 2.3 times greater, the velocity width is 1.9 times wider, and the velocity centroid is 0.3 times smaller if the systemic absorption is not removed. For the Mg II doublet, the EW is 1.7 times greater, the velocity width is 1.5 times wider, and the velocity centroid is 0.5 times smaller if the systemic absorption is not removed. Therefore, quantitative results can be *up to a factor of 2 to 3 different* if systemic absorption is not accounted for.

For lines without detectable absorption, we estimate the $2\sigma$ upper limit on the EW that could have been measured. This is complicated due to Mg II emission in many cases; Mg II emission is discussed further in Section 4.3 below.

We further test whether our measured Mg II absorption parameters are sensitive to the stellar absorption accounted for in our continuum fits by measuring Mg II absorption in continuum-normalized spectra both with and without stellar absorption included. We test the higher S/N X-ray AGN host galaxies and find that when Mg II emission is not present, the results are not sensitive to stellar absorption, as our method above accounts for all absorption at systemic, whether from stars or the ISM. However, the stellar absorption included in our continuum fits can affect the detected Mg II emission, in that one can underestimate the Mg II emission if stellar absorption is not accounted for (see Section 4.3).

## 4. RESULTS ON WINDS DETECTED IN ABSORPTION

In this section we first present results of fitting our spectra for Fe II, Mg II, and Mg I absorption, investigating which objects have outflowing winds as seen in blueshifted absorption and what the wind properties are. We then compare the different absorption lines. In the following section we present measurements of Mg II and Fe II* emission in each object, which likely originates in the wind as well (Weiner et al. 2009; Rubin et al. 2010; Prochaska et al. 2011).

### 4.1. *Outflowing Winds Detected in Absorption*

Figures 6-8 show details of the observed and continuum-normalized spectra for each galaxy in our sample centered on the Fe II, Mg II, and Mg I absorption lines. For each object we present two rows of plots: the upper row is the fluxed spectrum (black) and stellar continuum fit (red), while the lower panel is the continuum-normalized spectrum (black), with the continuum level (equal to unity) shown in green. These figures clearly show the variance seen among different objects in our sample in terms of the absorption line strengths and velocity profiles. The figures also illuminate the importance of accounting for stellar absorption at Mg II and Mg I in objects with older stars, as the continuum-normalized spectra often have features, such as Mg II in emission, that are not clearly seen in the observed spectra.

Table 5 lists the results of the absorption line fits and EWs of the Fe II, Mg II, and Mg I lines for each galaxy in our sample that has an outflowing or possibly inflowing wind with an EW detected at the $\geq 3\sigma$ level. We do not include objects in this table for which we did not measure a significant wind in absorption (after removing absorption at systemic), and we list for each object only those lines for which we had spectral coverage. For line doublets that were fit simultaneously, the velocity width of both lines is constrained to be identical. The quoted error on the Mg II outflow EW for galaxy 42020386 may be underestimated, as the error on the Mg II stellar continuum EW was 32%. However, this object also has significant absorption in Fe II, which is not affected by the stellar continuum fit.

Five of nine X-ray AGN host galaxies, plus the LIRG (object 22029058), have detected outflowing winds detected in absorption, for a total of six out of ten objects in this sample. Five of these galaxies are in the blue cloud, and their spectra (Figure 2) show strong nebular emission lines. The velocity centroids of the absorption features in these five galaxies are $\sim -200 - -500$ km s$^{-1}$, similar to the velocities found by Weiner et al. (2009) and Rubin et al. (2010) for star-forming galaxies at $z \sim 1$.

One galaxy in our X-ray AGN host galaxy sample, 13004312, shows tentative evidence for a much higher velocity outflow. The bluer Mg II line at 2796 Å has a Gaussian fit with a velocity centroid of $-1225$ km s$^{-1}$, with a width of $\sim 500$ km s$^{-1}$. The velocity profiles for Fe II 2599 Å, Mg II (the bluer 2796 Å line only), and Mg I for this object are shown in Figure 9. In this object Mg I does not have strong blueshifted absorption indicative of an outflow. The redder Mg II line at 2803 Å does not show absorption, due to Mg II emission and the presence of the bluer Mg II line. The absorption line fit at Fe II 2599 Å indicates a central velocity of $-550$ km s$^{-1}$ with a width of 157 km s$^{-1}$, but the EW measured is significant at only the $1.7\sigma$ level. The absorption at $\sim -1600$ km s$^{-1}$ seen in the Fe II line is due to Fe II absorption at 2587 Å. However, the Mg II 2796 Å line shows a wide blueshifted absorption trough, extending out to $\sim -2000$ km s$^{-1}$ before reaching the continuum level. We note that this is a red galaxy with an older stellar population (see Figure 2) with significant, broad stellar Mg II absorption. The absorption feature in Mg II shown in Figure 9 is apparent only after dividing out the stellar component (see Figure 6). This object also has clear Mg II emission (Mg II emission in the sample as a whole is discussed in detail in Section 4.3 below). The fractional error on the Mg II stellar absorption EW for this object is <1%, indicating that the profile seen af-

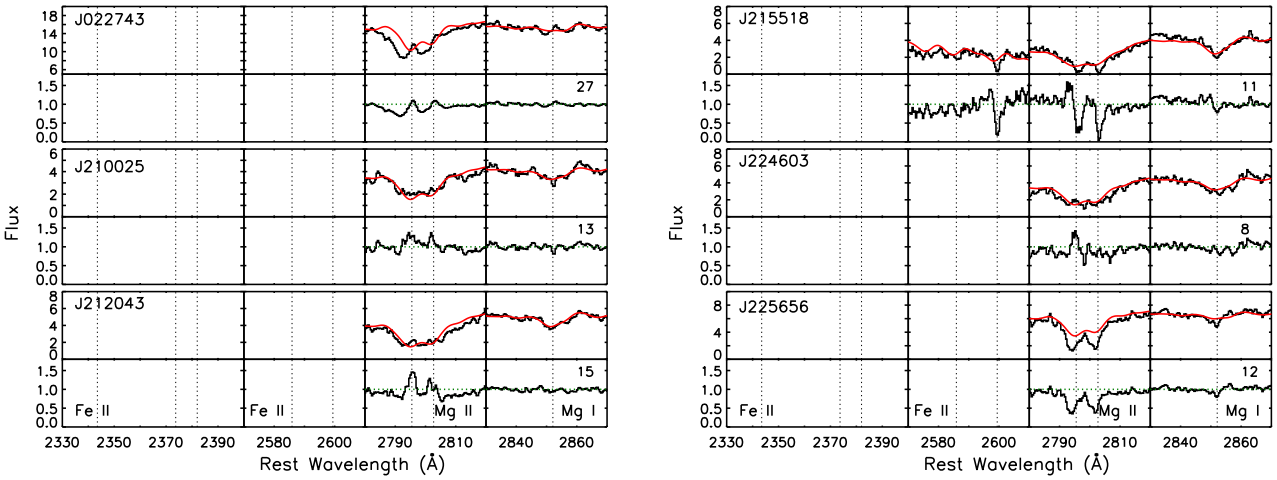


FIG. 8.— Regions of the observed and continuum-normalized spectra around Fe II, Mg II, and Mg I for objects in the SDSS K+A galaxy sample, similar to Figures 6 and 7.

ter removing stellar absorption is robust, in which case the extreme outflow detected in Mg II in this galaxy is also likely robust. As the Fe II 2599 Å line, which is less affected by stellar absorption, shows that there is likely a wind at $\sim -600$ km s$^{-1}$, this suggests that the Mg II profile is valid. We conclude that this object likely has an outflow with a central velocity of at least $\sim -600$ km s$^{-1}$ and may have a more extreme outflow in Mg II.

The typical velocity widths observed in the X-ray AGN sample are $\sim$100 – 300 km s$^{-1}$. We note that given the resolution of these data, the absorption lines are not resolved. The maximum velocity at which we detect blueshifted absorption is typically $\sim$500–800 km s$^{-1}$. The covering fractions that we measure are lower limits, given the resolution of our data, and are generally within the range of 0.1 – 0.5. The EWs span a range of values from 0.2 – 2.5 Å.

For our K+A samples, we detect outflowing winds in absorption in two of the seven DEEP2 objects and two of six SDSS objects. The velocity centroids of these four objects are between $-130$ – $-500$ km s$^{-1}$, with widths of 65 – 371 km s$^{-1}$. Given the resolution of our data, the lines are not resolved. The maximum velocities range from $-225$ – $-1192$ km s$^{-1}$. The covering fractions for the two SDSS K+A galaxies range from 0.1 – 0.6. For the DEEP2 K+A galaxies, the spectra are noisier (as the objects are much fainter) and the derived covering fraction can be greater than unity, though generally within the error bars they are consistent with unity. The EWs vary from 0.1 – 2.0 for the SDSS objects and 1.0 – 7.6 for the DEEP2 objects. We note that the presence of Mg II emission in many of these objects (discussed further in Section 4.3 below) may systematically affect our measurements of Mg II absorption (see also Prochaska et al. 2011).

On the whole, we detect winds via blueshifted Fe II, Mg II, and Mg I absorption for 43% of our sample. The velocity centroids of the winds are a few hundred km s$^{-1}$, much lower than the extreme winds seen by Tremonti et al. (2007), with the possible exception of one red X-ray AGN host galaxy which shows tentative evidence for an outflow with a centroid of $\sim -600$ – $-1200$ km s$^{-1}$.

Two K+A galaxies in our sample (42021012 and J215518) show possible evidence for gas *inflow* along the line of sight. Absorption line measures for these two sources are given in Table 5. For these two objects we have *not* corrected for systemic absorption, as the velocity centroids are often measured to be positive (redward of systemic), such that the absorption is not symmetric about the systemic velocity. Unlike for the other sources in this table, for these two objects we list the maximum *redshifted* velocity of the absorption for each line. For object 42021012, redshifted absorption is detected in both Mg I and Mg II, with a velocity centroid of 115 and 46 km s$^{-1}$, respectively. The absorption detected for the various Fe II lines is consistent with systemic. For object J215518 redshifted absorption is detected in Mg II, while blueshifted absorption is detected in a single Fe II line. We further note that object 32008909 (not included in this table) has a complicated Mg II absorption profile that may indicate both blueshifted and redshifted gas (see Figure 7). The redshifted gas seen in absorption in these sources could be inflowing cool gas from a galactic fountain, gas accretion due to minor mergers, or gas cooling from the halo of the galaxy. The relatively high EW ($\sim$1-2 Å) of the redshifted gas should constrain its

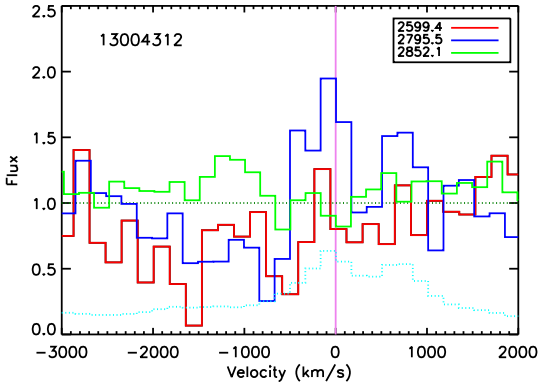


FIG. 9.— Absorption velocity profiles of Fe II 2599 Å (red), Mg II 2796 Å (blue), and Mg I 2582 Å (green) for object 13004312, a red X-ray AGN host galaxy that may have a high velocity outflow. The error spectrum for Mg II 2796 Å is shown in cyan.

TABLE 5
Fe II, Mg II, and Mg I Absorption Line Measurements and Equivalent Widths

| Line (Å) | Velocity centroid[1] (km/s) | Velocity width[2] (km/s) | Max. vel.[3] (km/s) | $A_{flow}$[4] | EW (Å) |
|---|---|---|---|---|---|
| DEEP2 X-ray AGN Host Galaxies | | | | | |
| 11046507 | | | | | |
| 2852.1 | X[5] | X | X | X | X |
| 2802.7 | −141 ±103 | 69 ±46 | −225 | 0.11 ±0.08 | 0.18 ±0.08 |
| 2795.5 | −279 ±44 | 115 ±45 | −505 | 0.13 ±0.04 | 0.42 ±0.11 |
| 2599.4 | −312 ±71 | 327 ±66 | −729 | 0.08 ±0.03 | 0.45 ±0.12 |
| 2585.9 | −312 ±71 | 327 ±66 | −782 | 0.11 ±0.02 | 0.64 ±0.13 |
| 2382.0 | X | X | X | X | X |
| 2373.7 | X | X | X | X | X |
| 2343.5 | −360 ±71 | 151 ±76 | −561 | 0.14 ±0.06 | 0.39 ±0.13 |
| 12016790 | | | | | |
| 2852.1 | −329 ±42 | 145 ±43 | −558 | 0.12 ±0.03 | 0.39 ±0.10 |
| 2802.7 | −297 ±10 | 170 ±9 | −653 | 0.37 ±0.10 | 1.40 ±0.09 |
| 2795.5 | −297 ±10 | 170 ±9 | −677 | 0.45 ±0.03 | 1.80 ±0.11 |
| 2599.4 | −255 ±16 | 264 ±16 | −822 | 0.38 ±0.14 | 2.20 ±0.13 |
| 2585.9 | −255 ±16 | 264 ±16 | −805 | 0.33 ±0.02 | 1.63 ±0.12 |
| 2382.0 | −177 ±18 | 138 ±16 | −451 | 0.52 ±0.07 | 1.48 ±0.17 |
| 2373.7 | −177 ±18 | 138 ±16 | −416 | 0.33 ±0.06 | 0.82 ±0.15 |
| 2343.5 | −253 ±41 | 209 ±42 | −612 | 0.36 ±0.06 | 1.26 ±0.17 |
| 13004312 | | | | | |
| 2852.1 | X | X | X | X | X |
| 2802.7 | X | X | X | X | X |
| 2795.5 | −1225 ±161 | 496 ±156 | −2136 | 0.47 ±0.13 | 3.07 ±0.77 |
| 2599.4 | X | X | X | X | X |
| 2585.9 | X | X | X | X | X |
| 13041622 | | | | | |
| 2852.1 | X | X | X | X | X |
| 2802.7 | −576 ±106 | 271 ±82 | −717 | 0.18 ±0.08 | 0.63 ±0.27 |
| 2795.5 | −576 ±106 | 271 ±82 | −913 | 0.17 ±0.05 | 1.21 ±0.28 |
| 13063920 | | | | | |
| 2852.1 | −136 ±48 | 92 ±38 | −263 | 0.13 ±0.05 | 0.25 ±0.08 |
| 2802.7 | −289 ±11 | 204 ±9 | −739 | 0.51 ±0.13 | 2.52 ±0.12 |
| 2795.5 | −289 ±11 | 204 ±9 | −741 | 0.49 ±0.03 | 2.17 ±0.13 |
| 2599.4 | −217 ±20 | 185 ±20 | −591 | 0.41 ±0.04 | 1.58 ±0.13 |
| 2585.9 | −152 ±15 | 126 ±18 | −409 | 0.42 ±0.05 | 1.10 ±0.11 |
| 2382.0 | −177 ±27 | 184 ±27 | −526 | 0.43 ±0.05 | 1.55 ±0.16 |
| 2373.7 | −102 ±33 | 133 ±32 | −326 | 0.31 ±0.07 | 0.80 ±0.15 |
| 2343.5 | −207 ±24 | 164 ±24 | −535 | 0.48 ±0.06 | 1.37 ±0.15 |
| 22029058 | | | | | |
| 2852.1 | −249 ±56 | 84 ±54 | −389 | 0.18 ±0.06 | 0.37 ±0.11 |
| 2802.7 | −314 ±11 | 169 ±10 | −675 | 0.49 ±0.14 | 1.87 ±0.14 |
| 2795.5 | −314 ±11 | 169 ±10 | −677 | 0.58 ±0.04 | 2.19 ±0.14 |
| 2599.4 | −141 ±14 | 175 ±15 | −499 | 0.55 ±0.19 | 1.89 ±0.15 |
| 2585.9 | −141 ±14 | 175 ±15 | −503 | 0.45 ±0.04 | 1.58 ±0.14 |

| Line (Å) | Velocity centroid (km/s) | Velocity width (km/s) | Max. vel. (km/s) | $A_{flow}$ | EW (Å) |
|---|---|---|---|---|---|
| DEEP2 K+A Galaxies | | | | | |
| 31046744 | | | | | |
| 2852.1 | X | X | X | X | X |
| 2802.7 | −82 ±30 | 103 ±30 | −225 | 1.45 ±0.37 | 2.48 ±0.59 |
| 2795.5 | −433 ±86 | 265 ±83 | −633 | 0.73 ±0.20 | 3.45 ±0.91 |
| 2599.4 | X | X | X | X | X |
| 2585.9 | −133 ±50 | 249 ±50 | −480 | 0.79 ±0.14 | 3.41 ±0.54 |
| 2382.0 | X | X | X | X | X |
| 2373.7 | X | X | X | X | X |
| 2343.5 | −161 ±38 | 135 ±38 | −356 | 0.73 ±0.17 | 1.76 ±0.36 |
| 42021012[6] | | | | | |
| 2852.1 | 115 ±34 | 73 ±35 | 200 | 0.40 ±0.16 | 0.72 ±0.28 |
| 2802.7 | 46 ±23 | 166 ±20 | 268 | 0.66 ±0.39 | 2.13 ±0.39 |
| 2795.5 | 46 ±23 | 166 ±20 | 311 | 0.75 ±0.10 | 2.58 ±0.40 |
| 2599.4 | 76 ±25 | 136 ±25 | 217 | 0.48 ±0.34 | 1.28 ±0.32 |
| 2585.9 | 76 ±25 | 136 ±25 | 286 | 0.65 ±0.12 | 2.03 ±0.37 |
| 2382.0 | 93 ±34 | 170 ±34 | 305 | 0.81 ±0.53 | 2.39 ±0.46 |
| 2373.7 | 93 ±34 | 170 ±34 | 292 | 0.47 ±0.13 | 1.47 ±0.44 |
| 2343.5 | 158 ±35 | 176 ±35 | 848 | 0.93 ±0.16 | 3.15 ±0.54 |
| 42020386 | | | | | |
| 2852.1 | X | X | X | X | X |
| 2802.7 | −258 ±23 | 69 ±22 | −353 | 0.97 ±0.29 | 1.02 ±0.49 |
| 2795.5 | −236 ±21 | 70 ±22 | −333 | 1.10 ±0.29 | 1.34 ±0.45 |
| 2599.4 | −167 ±17 | 81 ±18 | −268 | 0.70 ±0.20 | 1.65 ±0.43 |
| 2585.9 | −167 ±17 | 81 ±18 | −294 | 1.17 ±0.26 | 1.92 ±0.42 |
| 2382.0 | −109 ±32 | 89 ±32 | −224 | 1.29 ±0.40 | 2.29 ±0.62 |
| 2373.7 | X | X | X | X | X |
| 2343.5 | X | X | X | X | X |
| SDSS K+A Galaxies | | | | | |
| J022743 | | | | | |
| 2852.1 | −286 ±32 | 94 ±32 | −389 | 0.07 ±0.02 | 0.14 ±0.04 |
| 2802.7 | −386 ±15 | 138 ±15 | −632 | 0.23 ±0.02 | 0.71 ±0.07 |
| 2795.5 | −509 ±20 | 371 ±20 | −1192 | 0.27 ±0.02 | 2.00 ±0.08 |
| J215518[5] | | | | | |
| 2852.1 | X | X | X | X | X |
| 2802.7 | 75 ±15 | 100 ±14 | 225 | 0.92 ±0.30 | 1.92 ±0.25 |
| 2795.5 | 75 ±15 | 100 ±14 | 203 | 0.82 ±0.16 | 1.53 ±0.33 |
| 2599.4 | 30 ±24 | 89 ±23 | 102 | 0.81 ±0.39 | 1.64 ±0.40 |
| 2585.9 | X | X | X | X | X |
| J225656 | | | | | |
| 2852.1 | −224 ±66 | 130 ±65 | −305 | 0.10 ±0.04 | 0.22 ±0.09 |
| 2802.7 | −213 ±14 | 142 ±13 | −439 | 0.53 ±0.19 | 1.60 ±0.16 |
| 2795.5 | −213 ±14 | 142 ±13 | −441 | 0.60 ±0.06 | 1.71 ±0.18 |

[a]Velocity offset of center of Gaussian fit from systemic velocity
[b]Velocity width of Gaussian fit
[c]Maximum velocity used in EW measurement
[d]$A_{flow}$ is 1 - the minimum line depth of the outflow component and corresponds to a lower limit on the covering fraction for optically thick lines
[e]An 'X' indicates spectral coverage of this line but no significant outflowing or inflowing absorption is detected
[f]Possible 'inflow' object; EW measured for the observed absorption without a systemic component removed

origin; in particular, this may be higher than what is expected for gas cooling from the halo.

### 4.2. *Dependence of Mg II Absorption on Galaxy Properties*

In Figure 10 we compare the Mg II 2796 Å velocity centroid (left) and EW (right) with the galaxy $U-B$ color. Following Yan et al. (2009), who study K+A samples selected in both DEEP2 and SDSS, in this figure we put both samples on common ground by shifting the $U-B$ colors of the SDSS objects blueward by $\delta(U-B)$ =0.14 to account for passive evolution between the SDSS and DEEP2 samples. In the left panel, galaxies without detected blueshifted Mg II absorption are shown as triangles with velocities of 0 km s$^{-1}$, and in the right panel $2\sigma$ EW upper limits are shown for these objects.

Figure 10 shows that the detection rate of winds via blueshifted Mg II absorption is higher for the blue galaxies with $U-B < 1.0$. At $U-B \geq 1.0$ only two of the ten galaxies have winds detected in absorption. However, the spectral S/N is lower for the red galaxies, on the whole, such that some of the EW upper limits are not very constraining. Of the galaxies with winds de-

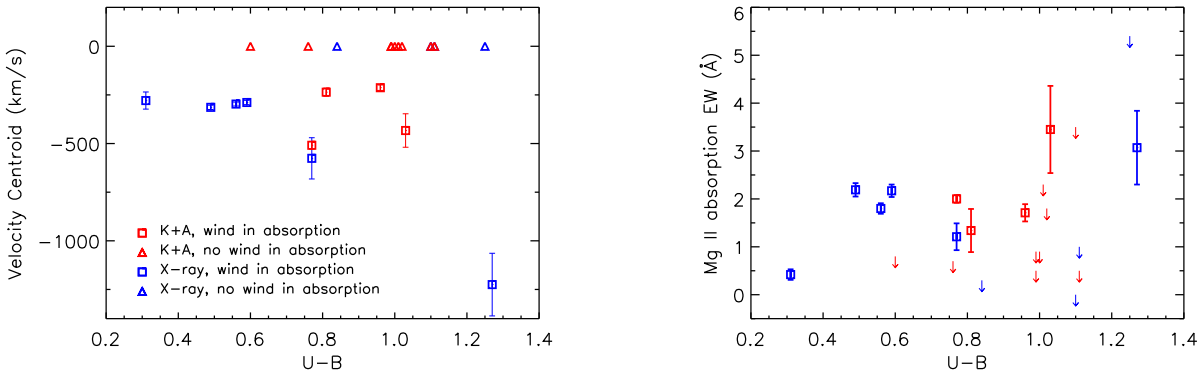


FIG. 10.— Velocity centroid (left) and equivalent width (right) of the Mg II 2795.5 Å absorption line versus restframe $U-B$ color for each object in our sample. The equivalent width shown is for the outflow component of the absorption line only, where any systemic contribution has been removed (see Section 3.2 for details). K+A galaxies are shown in red and X-ray AGN host galaxies are shown in blue. Galaxies without blueshifted Mg II absorption are shown as triangles. We have subtracted $U-B$ =0.14 from the colors of the SDSS K+A galaxies to match the colors of the DEEP2 galaxies and remove the effects of passive evolution. In the right panel $2\sigma$ upper limits on the EW are given for objects without detected blueshifted absorption.

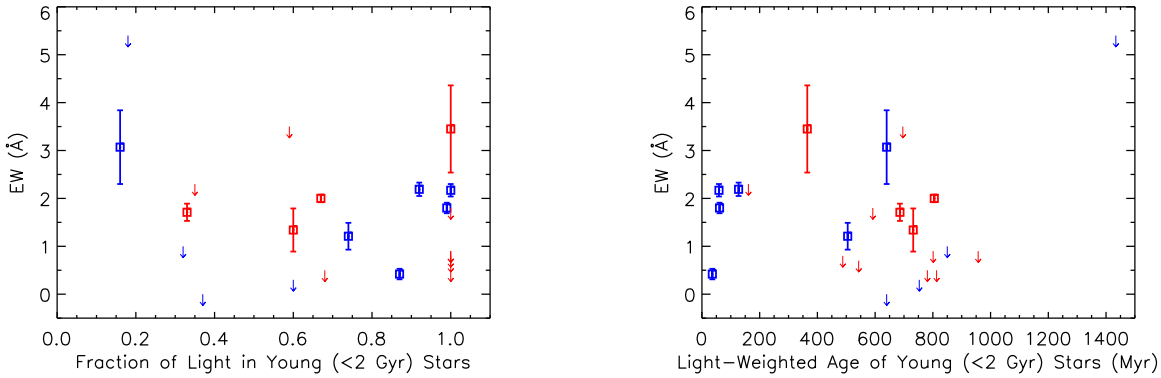


FIG. 11.— EW of the Mg II 2795.5 Å absorption line versus the fraction of light in young (<2 Gyr) stars (left) and the light-weighted age of the young stars (right). As in the previous figure, the equivalent width shown is for the outflow component of the absorption line only, where any systemic contribution has been removed. K+A galaxies are shown in red and X-ray AGN host galaxies are shown in blue. $2\sigma$ upper limits on the EW are given for objects without detected blueshifted absorption.

tected in absorption, we do not find a strong correlation between the velocity centroid and the galaxy color, with the exception of the single red galaxy with a high velocity outflow. The apparent trend in the right panel that the EW is higher for redder galaxies may be a selection effect, as due to the lower S/N of the red galaxy spectra we would not be able to detect low EW outflows.

We find that the velocity centroids and EWs of the Mg II absorption are similar for the AGN host galaxies and the K+A galaxies; within our small samples, neither population appears to have faster winds or higher EW winds. This is discussed further in Section 6.3 and 6.4.

In Figure 11 we investigate the correlation of the Mg II 2796 Å absorption EW with the light-weighted age of the stars in the galaxy, comparing with the fraction of light due to young (<2 Gyr) stars on the left and the light-weighted age of the young stars on the right. Most (7/9) detected winds in absorption are seen in galaxies with more than 50% of their light due to young stellar populations. Within that population, however, we do not find a correlation between EW and the fraction of light in young stars. Similarly, all detections are in galaxies in which the young stars have an age less than 800 Myr, though we do not find a correlation between EW and age of the young stars. We do find that the detection fraction is a function of the light-weighted age of the young stars, with higher detection fractions found for younger stellar populations. For the K+A galaxies in our sample, the light-weighted age of young stars may be interpreted roughly as the time since the last episode of star formation, and the observed trend is that the likelihood of detecting a wind lowers once the time since the last burst is $\gtrsim$500 Myr. The five X-ray AGN host galaxies in this figure with light-weighted young ages <500 Myr have blue colors and emission lines indicative of on-going star formation, however, such that the light-weighted age is not strictly the time since the last episode of star formation.

### 4.3. *Comparison of Absorption Lines*

We next study the absorption seen at Fe II, Mg II, and Mg I on an object-by-object basis, comparing the absorption profiles and Gaussian fit results from the different ions and ionization states. Figure 12 shows the velocity profile of each line for two of the X-ray AGN host

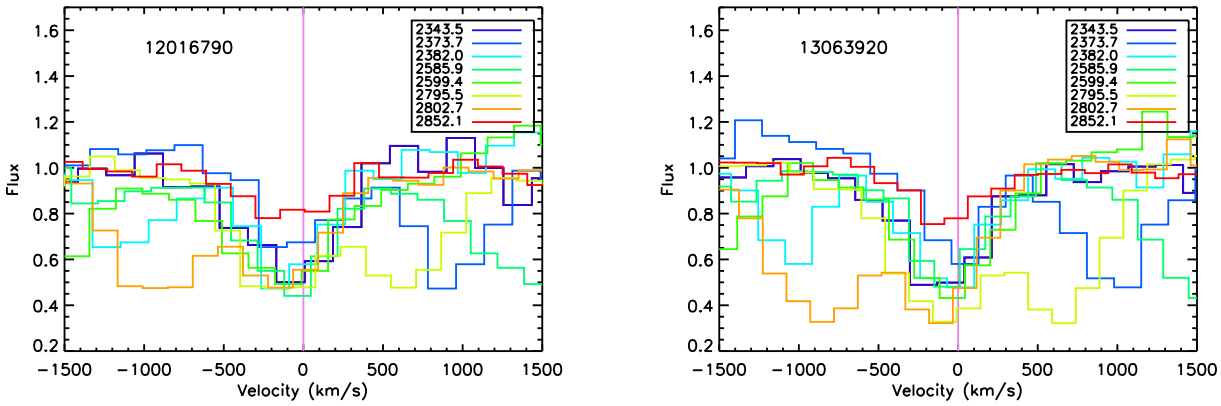


FIG. 12.— Comparison of the absorption profiles for all Fe II, Mg II, and Mg I lines covered for two objects with high S/N in our X-ray AGN host galaxy sample. We show the observed spectra here, without removing the systemic component.

galaxies in our sample. Each line of the Mg II doublet (which has a velocity separation of 770 km s$^{-1}$) is shown in green-yellow and orange colors, which causes the absorption at $\sim -900$ km s$^{-1}$ in orange and $+600$ km s$^{-1}$ in green-yellow. The two spectra shown here have relatively high S/N, which facilitates a by-eye comparison of their absorption troughs. Clearly at this resolution the general shape is very similar between Fe II, Mg II, and Mg I, though the minimum line depth can vary between the lines, with Mg I having less absorption in both of the objects shown. For Mg I the lower absorption could be due either to a lower covering fraction or a lower optical depth or both. As Mg I is a singlet we can not distinguish between these scenarios, unlike for the Mg II doublet, which is saturated and therefore optically thick. The line profiles for the Fe II transitions are similar with each other and with Mg II, indicating that the lines are either saturated or nearly so (e.g., Martin & Bouche 2009).

Figure 13 quantitatively compares the results in Table 5 for the absorption line measurements—central velocity, velocity width, covering fraction, and EW—among the different lines for individual objects. Here we treat the $A_{flow}$ values listed in Table 5 as the covering fraction. The left panel compares Mg I with the bluer Mg II line, while the right panel compares Fe II 2599.4 Å with the bluer Mg II line. We have also compared (but do not show) the various Fe II lines against each other. We find that the velocity centroids, velocity widths, covering fractions and EWs all agree reasonably well both between the various Fe II lines and between the Fe II lines and the bluer Mg II line, within the measured errors. The covering fraction of Fe II 2599.4 Å appears to be systematically slightly lower than for Mg II. We do not consider the redder Mg II line in this comparison as the absorption trough may be affected by the bluer Mg II line.

In comparing Mg I and Mg II, we find that Mg I has a significantly lower covering fraction and/or optical depth and a lower EW (which is closely tied to the covering fraction in our unresolved data) than either Mg II or Fe II. Additionally, Mg I often has a lower velocity centroid and width than either Mg II or Fe II. As Mg I has a lower ionization potential than Mg II, 7.6 eV compared to 15.0 eV, it is likely that Mg I traces denser gas in smaller clumps, which have a lower covering fraction. Weiner et al. (2009) also found that the EW and covering fraction of Mg I was smaller than Mg II in DEEP2 star-forming galaxies at $z \sim 1.4$.

Comparing the various Fe II lines with each other, we find that 2599.4 Å and 2585.9 Å agree well in terms of velocity centroid, velocity width, and covering fraction, while the EW of 2599.4 Å is generally slightly higher than 2585.9 Å. Comparing Fe II 2599.4 Å with 2343.5 Å, we find that both lines agree well in terms of velocity centroid and covering fraction, while for velocity width and EW 2599.4 Å is a bit higher than 2343.5 Å. However, our sample size for this comparison is only a few data points, making robust conclusions difficult. We stress again that these data are not high resolution, which one would ideally want for this kind of comparison. Additionally, there can be emission systematically affecting our measurements, for Mg II in particular (discussed below).

### 4.4. *Na D*

The LRIS spectra for our SDSS K+A sample extend far enough in the red to cover the Na D 5889.95, 5898.92 Å doublet, which is often used in low redshift galaxies to search for winds. In our two SDSS K+A galaxies in which we detect winds in Mg II absorption, we find that in one object (J022743) there is strong emission at Na D, centered on the systemic velocity. In the other object (J225656) we find evidence for an outflowing wind in the Na D absorption profile. In our other four SDSS K+A galaxies Na D either is seen in emission at the systemic velocity or has no detected emission or absorption.

As Na D is a resonance absorption transition, if Na D is absorbed along certain sight lines due to an anisotropic wind (e.g., a biconical outflow), this can lead to isotropic Na D emission. Na D emission is observed by Chen et al. (2010) in their SDSS sample of star-forming galaxies, primarily in face-on galaxies with little dust. They suggest that the Na D emission is from the back side of an expanding bipolar outflow. They also note that for some objects the emission is observed only after dividing out the stellar continuum; this is also the case for our object, J022743. As discussed in detail in Chen et al. (2010), while one cannot rule out continuum fitting errors, the emission may be real and from the wind itself.

In object J225656 the Na D doublet is consistent with

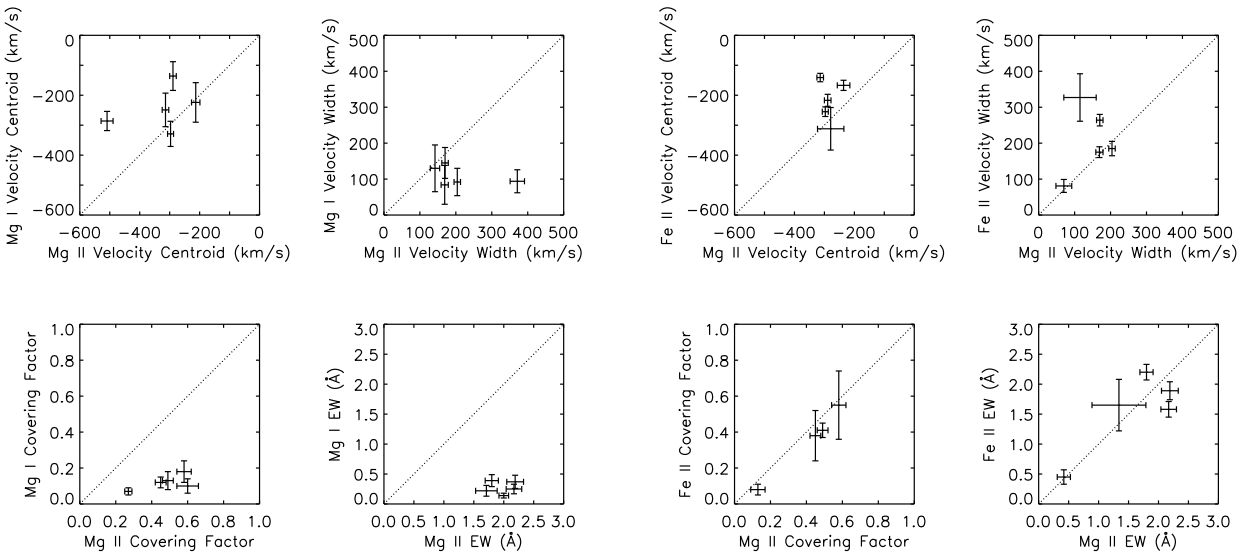


FIG. 13.— Comparison of absorption line fits for Mg I 2852.1 Å versus Mg II 2795.5 Å (left) and Fe II 2599.4 Å versus Mg II 2795.5 Å (right).

a wind with the same velocity parameters found from the Mg II and Mg I lines: the velocity centroid is −158 km s$^{-1}$ with a width of 81 km s$^{-1}$. The covering fraction is 0.07 ±0.01, similar to what is found for Mg I (0.10 ±0.04) and lower than Mg II (0.53-0.60).

## 5. RESULTS ON WINDS DETECTED IN EMISSION

We now turn to emission line detections of outflowing winds in our sample, studying detections of both Mg II and Fe II* emission in our spectra.

### 5.1. *Mg II Emission*

To observe Mg II emission, there must be scattered emission that is not re-absorbed; to produce such emission it therefore helps if there is a velocity gradient and non-isotropic illumination of the gas (e.g., outflowing material illuminated by a central source, observed along a sight line to the gas but not the central source). Mg II emission is not generally seen in H II regions, as it is disfavored by a factor of the abundance. As discussed in Weiner et al. (2009) and Rubin et al. (2011), Mg II can often be seen in both emission and absorption with a P-Cyngi-type profile in objects with outflowing winds, where the emission component is presumably from the back side of the wind (see also Phillips 1993, for an example in Na I). This idea is modeled by Prochaska et al. (2011) using radiative transfer calculations for a simple wind model. Using this model they predict that the emission EW should equal the absorption EW for a galaxy with little dust and an isotropic outflow which is fully covered by the spectrograph slit; in the presence of dust the emission EW decreases.

We show in Figure 14 the region around Mg II for each of the objects in our sample. As can be seen in the figure, there is a wide range of Mg II profiles and properties, ranging from what appears to be pure emission to pure absorption. Table 6 lists emission line measurements for those objects with significant ($> 2\sigma$) Mg II emission detected above the continuum level. To determine these measurements we fit double Gaussian line profiles

TABLE 6
MG II EMISSION LINE MEASUREMENTS AND EQUIVALENT WIDTHS

| Object | Velocity centroid (km/s) | Velocity width (km/s) | 2795.5 Å EW (Å) | 2802.7 Å EW (Å) |
|---|---|---|---|---|
| DEEP2 X-ray AGN Host Galaxies | | | | |
| 11046507 | 238 ±100 | 174 ±99 | −0.43 ±0.12 | <0.24[1] |
| 13004312 | −83 ±76 | 151 ±68 | −3.83 ±1.80 | −2.02 ±1.51 |
| 13025528 | −88 ±40 | 235 ±30 | −12.46 ±1.99 | −8.84 ±1.88 |
| 13043681 | 16 ±126 | 107 ±104 | −5.09 ±3.47 | −11.22 ±3.90 |
| 13051909 | −155 ±52 | 212 ±40 | −3.22 ±0.73 | −2.57 ±0.66 |
| DEEP2 K+A Galaxies | | | | |
| 32003698 | 290 ±53 | 205 ±42 | −7.70 ±2.59 | −6.47 ±1.58 |
| 43030800 | 39 ±25 | 68 ±24 | −3.11 ±0.87 | <1.88 |
| SDSS K+A Galaxies | | | | |
| J022743 | 46 ±13 | 51 ±13 | −0.14 ±0.04 | −0.17 ±0.04 |
| J210025 | −70 ±28 | 102 ±27 | −1.17 ±0.28 | −0.63 ±0.22 |
| J212043 | 19 ±21 | 80 ±22 | −0.98 ±0.24 | −0.38 ±0.19 |
| J215518 | −260 ±36 | 85 ±34 | −0.95 ±0.41 | <0.82 |

[a] $2\sigma$ upper limits are given for the few objects in which the redder Mg II line was not detected.

in emission, where the two lines were constrained to have the same velocity width. To obtain fits to the Mg II emission lines we use data within ±40 Å of the observed wavelength corresponding to the systemic velocity of each line in the doublet. This corresponds to roughly ∼3600 km s$^{-1}$ for the $z \sim 0.2$ objects and ∼2400 km s$^{-1}$ for the $z \sim 0.8$ objects. EWs are measured within the velocity range where the Gaussian fit is within 1% of the continuum level of the spectrum. Eight of the objects listed have Mg II emission detected at $> 3\sigma$, while another three objects have emission detected at a significance between $2\sigma$ and $3\sigma$. We detect Mg II emission in half of our sample: five of the ten X-ray AGN host galaxies and six of the thirteen K+A galaxies. The velocity centroids are consistent (less than $3\sigma$ deviant) with the systemic velocity for seven of the galaxies, while two galaxies have

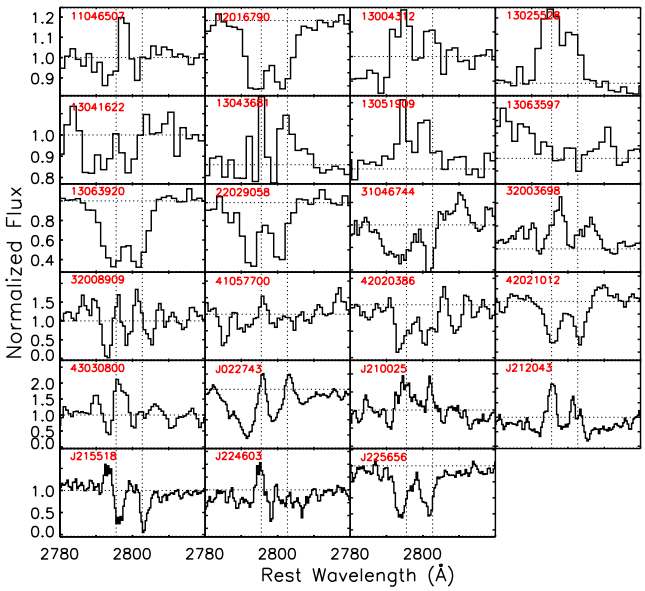


FIG. 14.— Region around the continuum-normalized Mg II flux for each object in our sample. The y-axis range varies for each object. There is a wide range of Mg II properties, ranging from strong absorption to strong emission. The K+A spectra have been smoothed by a boxcar of width three pixels for this figure.

blueshifted emission and two have redshifted emission. Presumably the redshifted emission is from the back side of the wind, while the blueshifted emission is from the front side of the wind (possibly in galaxies with dust that obscures the back side) and the emission at systemic is integrated over the entire geometry of the wind.

Of the eleven sources with emission detected in Mg II, three have detected blueshifted Mg II absorption as well and eight do not. The eight galaxies with Mg II emission but no blueshifted absorption are all either in the green valley or on the red sequence; they are not star-forming galaxies. This implies that the Mg II emission is not from young stars. All three of the galaxies in our sample that lie on the red sequence (all of which are X-ray AGN host galaxies) have Mg II emission detected (one at $2\sigma$ and two at $3\sigma$).

We looked in detail at all objects with Mg II emission that had potentially large continuum errors to verify whether the emission could be due to errors in the stellar continuum fit. Object 13051909, an X-ray AGN host galaxy on the red sequence, has a Mg II stellar absorption EW error of 20%. Normalizing the observed spectrum by a stellar continuum fit that has a Mg II EW that is low by $\sim 1\sigma$ results in Mg II emission in the continuum-normalized spectrum significant at the $2.6\sigma$ level; we conclude that the Mg II emission in this object is likely real. Within the DEEP2 K+A sample, object 43030800 (also on the red sequence) has a 26% error in the Mg II stellar absorption EW. Repeating the above test of renormalizing the observed spectrum by a stellar continuum fit that is low by $\sim 1\sigma$ results in Mg II emission significant at the $\sim 2\sigma$ level. For the other DEEP2 K+A galaxy with Mg II emission, the DEIMOS Mg II stellar EW is within 6% of the LRIS Mg II stellar EW, such that the continuum error is subdominant.

For the SDSS sample, as discussed above the statistical errors in the continuum fits are negligible. However, as systematic errors in the continuum fits to the LRIS spectra could lead to overestimated emission, we checked all of these objects in detail. In J022743, the Mg II profile for this object shows a P-Cygni signature, indicating that the Mg II emission in likely real. For J210025, the Mg II stellar EW in the SDSS fit is larger than in the LRIS fit, such that using the SDSS stellar continuum fit would only lead to more emission in the continuum-normalized spectrum. For J212043 and J215518, the fractional difference in the Mg II stellar EWs in the SDSS and LRIS fits are well within the errors on the quoted Mg II emission in the continuum-normalized spectra. We therefore conclude that the Mg II emission in all of these objects is likely real.

Weiner et al. (2009) find that from their parent sample of $\sim$1500 star forming galaxies at $z = 1.4$, $\sim$50 galaxies have detected Mg II emission. These galaxies tend to be bright and blue, lying in the bluer half of the blue cloud with $U - B < 0.6$ (see their Figure 7). Their selection criteria of objects with Mg II emission may have selected the source with the highest emission EW, however, and so may not be directly comparable with the selection used here. We note that if the presence of Mg II emission is correlated with a lack of dust (Prochaska et al. 2011), then it is plausible that both the bluest and reddest galaxies would show Mg II emission, as these are the galaxies expected to have less dust. If this emission is indeed from the back side of the wind, including the objects in which Mg II is detected in emission raises the fraction of our sample with detected winds to 83% (19/23), including nine of the ten X-ray AGN host galaxies and nine of the thirteen K+A galaxies.

As discussed in Prochaska et al. (2011), the presence of Mg II emission can affect the Mg II absorption profile, which we use to measure kinematic properties of the outflow. The presence of emission line filling can bias the absorption line fits in that it can lower the measured EW, shift the velocity centroid to larger values, and lower the velocity width. The effect is lessened or absent in the Fe II lines, however, and given the good agreement between the kinematics observed in the different ions in section 4.1.2, it is likely not a major effect here.

We note that the EW observed in the bluer Mg II 2795.5 Å line in our sample is generally larger than the EW observed in the redder 2802.7 Å line. This is quantified in the left panel of Figure 15, which compares the EWs of the two emission lines. The median ratio of the 2795.5 Å EW relative to the 2802.7 Å EW is 1.4. This difference between the EWs of the two Mg II emission lines is also seen in the coadded spectra of star-forming DEEP2 galaxies in Weiner et al. (2009) and is not generally predicted by the models put forth in Prochaska et al. (2011). The only model presented in which the 2795.5 Å EW is larger than the 2802.7 Å line is their "$\phi = 0°$ model", in which the wind is anisotropic and hemispherical, where half of the sphere has a wind and half does not, and the wind is viewed from an angle such that the source is not covered ($\phi = 180°$ corresponds to the source being covered). However, in this model there is no Mg II absorption, which is seen in our data. This observed ratio of 2795.5 Å EW to 2802.7 Å EW in the data presented here and elsewhere is clearly a strong ob-

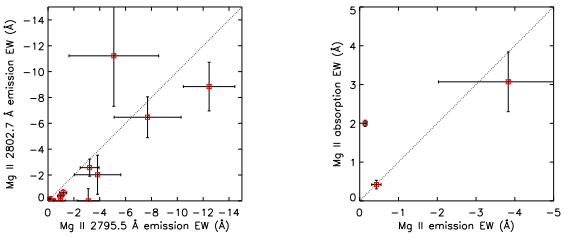


FIG. 15.— Left: Comparison of Mg II emission EW in the 2802.7 Å line with the 2795.5 Å line. Most objects have higher EW in the bluer Mg II line. Right: Comparison of the EW of Mg II 2795.5 Å in emission with the EW of Mg II 2795.5 Å in absorption for the three objects in which both are detected. Two of the objects have equal EWs in emission and absorption, while one has much stronger absorption than emission.

servational constraint on future, more sophisticated wind models.

We also note that several K+A galaxies in our sample (32003698, 43030800, J215518) show what appears to be emission blueward of the absorption seen at Mg II 2795.5 Å. While such a signature could in theory originate as emission from the front side of an extended wind, for two of these sources – 32003698 and J215518 – this emission may be a residual from the stellar absorption fit, while in the remaining source (43030800) given the S/N of the data we conclude that this emission may not be significant.

### 5.2. *Mg II Emission Versus Absorption*

In the right panel of Figure 15 we compare the Mg II 2795.5 Å absorption and emission EWs for the three objects in which both absorption and emission are detected at greater than $2\sigma$ for this line. We compare the bluer Mg II line as the absorption in the redder line can be seriously affected by emission in the bluer line. We find that two of the three objects have absorption and emission EWs that are consistent with each other, while one object (40602938) has a much higher absorption EW than emission EW. As discussed in Prochaska et al. (2011), the ratio of the absorption and emission EW of Mg II can depend both on the opening angle of the wind and the orientation of the wind relative to the observer, as well as the amount of dust in the galaxy. The two EWs will be roughly equal if the wind is isotropic or if an anisotropic, biconical wind with a large opening angle is observed 0° from the axis of rotational symmetry (i.e. along the cone), in the absence of dust. Obtaining absorption and emission EWs for much larger samples of objects should therefore help to constrain the geometry of the outflowing wind. Following the model of Prochaska et al. (2011), the one object observed here with a much higher absorption EW than emission EW should have $\tau_{dust} \gtrsim 3$, where $\tau_{dust}$ is the integrated opacity of dust from the center of the system. However, we note that this object (40602938) is fairly blue and is the bluest of the SDSS K+As, which, at least superficially, contradicts the idea of a high opacity dust screen.

### 5.3. *Fe II* Emission*

In addition to emission from Mg II, emission from Fe II* non-resonant fine structure lines has also been observed in galaxies at $z \sim 0.5 - 1$ that have outflowing winds. Rubin et al. (2011) present observations of Fe II* emission at 2364.8, 2395.6, 2611.9, and 2625.7 Å in a bright starburst galaxy at $z = 0.69$ that has a star formation rate $\sim$80 $M_\odot$ yr$^{-1}$. The galaxy has a wind detected in Mg II and Fe II absorption with a central velocity of $\sim -200 - -300$ km s$^{-1}$. They find that the Fe II* emission is at or near the systemic velocity of the galaxy, slightly redward of nebular lines such as [Ne III], H$\delta$, and H$\gamma$, and propose that the emission originates from photon scattering in the outflowing wind. Unlike the Mg II resonant line, blueshifted Fe II* line emission is not absorbed and therefore the line is expected to be at the systemic velocity if the wind is symmetric and dust in the galaxy is not obscuring the back side of the wind. They present alternative possible origins, including emission from gas in the galaxy disk as opposed to the gas in the outflowing wind, but conclude that the emission is most likely from the wind, due to differences in the emission line profile of Fe II* compared to nebular lines.

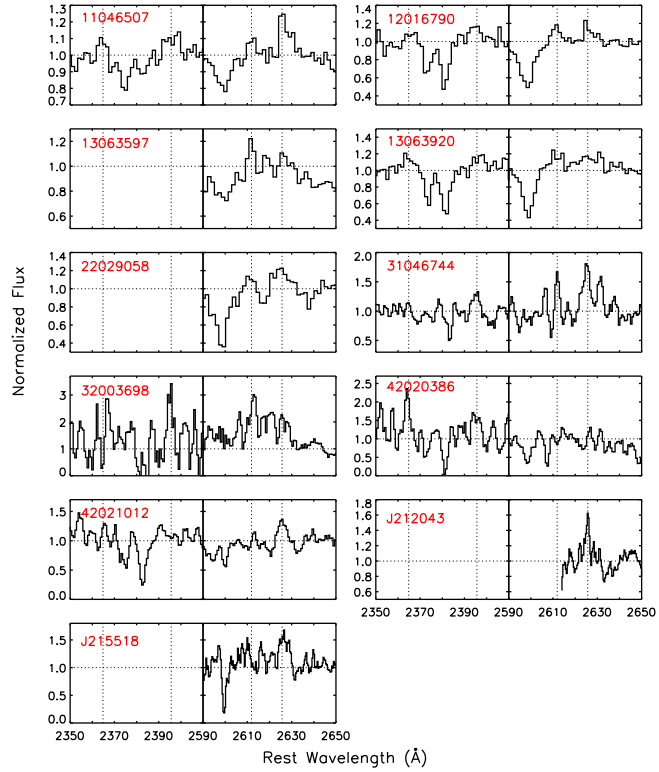


FIG. 16.— Region around Fe II* lines for each object in our sample in which we detect significant Fe II* emission. The wavelengths of the Fe II* lines are shown with dotted vertical lines corresponding to 2625.6679, 2611.8743, 2395.6263, and 2364.8292 Å. Note that the y-axis range varies between objects. The K+A spectra have been smoothed by a boxcar of width three pixels for this figure.

Here we investigate Fe II* emission in our sample for these same transitions. As with the Mg II emission lines, to obtain Gaussian fits to the Fe II* emission lines we use data within ±40 Å of the observed wavelength corresponding to the systemic velocity. This corresponds to roughly $\sim$4000 km s$^{-1}$ for the $z \sim 0.2$ objects and $\sim$2500 km s$^{-1}$ for the $z \sim 0.8$ objects. EWs are measured within the velocity range where the Gaussian fit is within 1% of the continuum level of the spectrum.

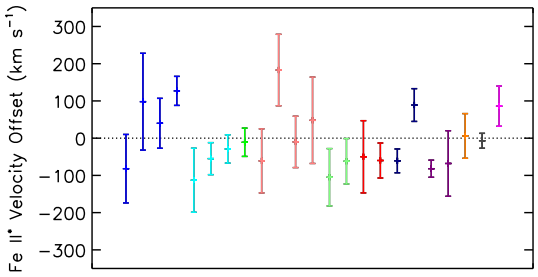


FIG. 17.— Velocity offset from the systemic velocity of the galaxy for each detected Fe II* emission line in our spectra. Different lines observed in the same object are shown with the same color. All but two of the observed Fe II* emission lines are within $2\sigma$ of the systemic velocity of the galaxy.

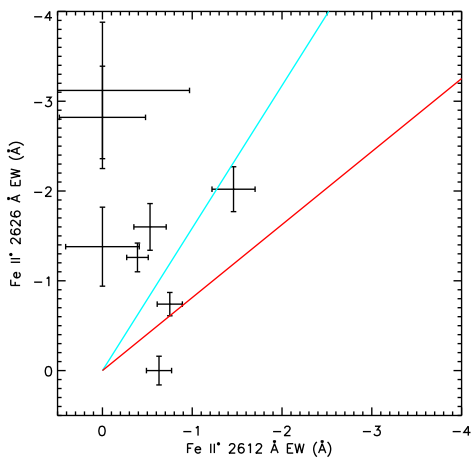


FIG. 18.— Comparison of the Fe II* 2611.9 Å EW to the Fe II* 2625.7 Å EW. Data points from our spectra are shown with error bars. The red and cyan lines show the extreme ratios predicted by the models of Prochaska et al. (2011).

Table 7 lists emission line measurements and EWs for Fe II* as well as [Ne III] and H$\zeta$. Not all of our spectra have the wavelength coverage to include all of these transitions; these are marked with ellipses in the table. Transitions where no significant emission is observed are marked with an 'X'. We include [Ne III] and H$\zeta$ as nebular comparison lines. By definition, the K+A galaxies will not have detected H$\zeta$ emission. Figure 16 shows the region around the various Fe II* lines for each object in which it is detected. Note that not all objects include spectral coverage of the bluest lines.

We detect significant Fe II* emission in five of the ten X-ray AGN host galaxies and six of the thirteen K+A galaxies. However, only two of the six SDSS K+A galaxies have blue enough spectral coverage to observe the Fe II* 2625.7 Å line, and Fe II* is detected in both of them, so it is entirely possible that the fraction of K+A galaxies with Fe II* emission is higher.

In the objects where H$\zeta$ is detected, it is always consistent with the systemic velocity. [Ne III] is at the systemic velocity in three out of six objects, blueshifted in one object, and redshifted in two objects. Similarly, each of the observed Fe II* lines is consistent at $2\sigma$ with the systemic velocity in all but two lines. The median velocity centroid observed among all of the Fe II* lines in galaxies in our sample is $-29$ km s$^{-1}$, while the median error of 61 km s$^{-1}$. Figure 17 shows the velocity offset from systemic of the velocity centroids for all measured Fe II* lines in Table 7. The velocity centroids measured from different Fe II* lines in the same object are generally consistent with each other. Our finding that the Fe II* emission is centered on the systemic velocity of the galaxy is consistent with the results of Rubin et al. (2011) and the models of Prochaska et al. (2011).

Additionally, we detect Fe II* emission in many of our K+A galaxies, which have little to no nebular emission and are not currently forming stars. It is therefore unlikely that the Fe II* emission in these galaxies arises from gas in the disk of the galaxy itself.

We compare the ratio of EW in the Fe II* 2611.9 Å and 2625.7 Å lines in our objects in Figure 18. Our data points with errors are shown in black, along with two models from Prochaska et al. (2011) that illustrate the minimum and maximum ratios found for these lines in their model. The maximum ratio predicted in their models is 1.23, which is for an anisotropic wind without dust (shown as a red line). The minimum ratio predicted is 0.63, which is for a model with an ISM component included (shown as a cyan line). Most of our objects have a ratio less than 0.5, where we have included objects that do not have emission detected at Fe II* 2611.9 Å. We have not included object 32003698 in this figure, as the emission detected at 2611.9 Å has a broad emission component which leads to a stronger observed EW but is not consistent with the simple wind models from Prochaska et al. (2011). We note that many of our objects do not fall within the allowed bounds of the models in Prochaska et al. (2011). Data are needed (at higher S/N) on many more objects, but these few examples show that measurements of this kind have the potential to be strongly constraining for theoretical wind models.

### 5.4. *Fe II* Emission Versus Mg II Emission*

Three objects in our sample have detected emission in both Mg II and Fe II*. We calculate the ratio of the emission line EW in Mg II 2795.5 Å to either the Fe II* 2611.9 or 2625.7 Å lines in two of these objects, as these line ratios should contain information about the physical conditions in the outflowing gas. In object 11046507 the ratio of 2795.5 Å EW to 2611.9 Å EW is 1.10 $\pm$0.17, while the ratio of 2795.5 Å EW to 2625.7 Å EW is 0.34 $\pm$0.20. In object 71633703 the ratio of 2795.5 Å EW to 2625.7 Å EW is 0.34 $\pm$0.70. In most of the models (fiducial model and variants) presented in Prochaska et al. (2011) the ratio of 2795.5 Å to 2611.9 Å varies from $\sim 2.9 - 14.6$, all higher than what we find here. The 'ISM' wind model predicts a ratio of 1.5, closer to what is found here. The models predict a ratio of 2795.5 Å to 2625.7 Å of $\sim 0.9 - 18$, significantly higher than what is found for our two objects. As in the case of the ratio of Fe II* EWs discussed above, these line ratios have the potential to constrain future theoretical models.

## 6. DISCUSSION AND CONCLUSIONS

TABLE 7
Fe II*, [Ne III], and Hζ Emission Line Measurements and Equivalent Widths

| Line (Å) | Velocity centroid (km/s) | Velocity width (km/s) | EW (Å) |
|---|---|---|---|
| DEEP2 X-ray AGN Host Galaxies | | | |
| 11046507 | | | |
| 2364.8 | −81 ±92 | 161 ±90 | −0.39 ±0.16 |
| 2395.6 | 99 ±130 | 373 ±128 | −0.79 ±0.23 |
| 2611.9 | 40 ±67 | 168 ±67 | −0.39 ±0.12 |
| 2625.7 | 126 ±39 | 255 ±39 | −1.26 ±0.16 |
| 3868.8 | 52 ±12 | 165 ±12 | −6.00 ±0.41 |
| 3889.1 | −12 ±13 | 166 ±12 | −6.19 ±0.44 |
| 12016790 | | | |
| 2364.8 | X[1] | X | <0.44 |
| 2395.6 | −112 ±86 | 299 ±86 | −0.99 ±0.25 |
| 2611.9 | −54 ±43 | 185 ±43 | −0.75 ±0.14 |
| 2625.7 | −29 ±38 | 169 ±37 | −0.74 ±0.13 |
| 3868.8 | X | X | X |
| 3889.1 | 11 ±10 | 105 ±10 | −1.93 ±0.17 |
| 13063597 | | | |
| 2364.8 | ...[2] | ... | ... |
| 2395.6 | ... | ... | ... |
| 2611.9 | −11 ±38 | 117 ±32 | −0.63 ±0.14 |
| 2625.7 | X | X | <0.32 |
| 3868.8 | −144 ±53 | 199 ±53 | −0.30 ±0.06 |
| 3889.1 | 11 ±10 | 226 ±10 | −2.58 ±0.10 |
| 13063920 | | | |
| 2364.8 | −60 ±86 | 275 ±86 | −0.92 ±0.24 |
| 2395.6 | 184 ±96 | 318 ±95 | −0.98 ±0.27 |
| 2611.9 | −10 ±69 | 342 ±69 | −1.46 ±0.24 |
| 2625.7 | 47 ±116 | 654 ±146 | −2.02 ±0.25 |
| 3868.8 | −13 ±38 | 128 ±37 | −0.56 ±0.13 |
| 3889.1 | −13 ±13 | 129 ±13 | −2.37 ±0.21 |
| 22029058 | | | |
| 2364.8 | ... | ... | ... |
| 2395.6 | ... | ... | ... |
| 2611.9 | −105 ±77 | 165 ±78 | −0.53 ±0.18 |
| 2625.7 | −63 ±61 | 302 ±61 | −1.60 ±0.26 |
| 3868.8 | −86 ±43 | 304 ±58 | −1.55 ±0.15 |
| 3889.1 | −32 ±14 | 171 ±15 | −2.53 ±0.17 |
| DEEP2 K+A Galaxies | | | |
| 31046744 | | | |
| 2364.8 | X | X | <1.42 |
| 2395.6 | −49 ±97 | 163 ±97 | −1.13 ±0.56 |
| 2611.9 | X | X | <1.95 |
| 2625.7 | −61 ±47 | 182 ±47 | −3.12 ±0.76 |
| 3868.8 | 0 ±22 | 61 ±22 | −0.93 ±0.32 |
| 3889.1 | X | X | X |
| 32003698 | | | |
| 2364.8 | X | X | <3.17 |
| 2395.6 | −60 ±32 | 120 ±32 | −6.83 ±1.60 |
| 2611.9 | 89 ±44 | 225 ±43 | −10.05 ±1.59 |
| 2625.7 | X | X | <1.82 |
| 3868.8 | X | X | X |
| 3889.1 | X | X | X |
| 42020386 | | | |
| 2364.8 | −81 ±23 | 79 ±22 | −3.36 ±0.87 |
| 2395.6 | −67 ±88 | 208 ±88 | −2.47 ±1.11 |
| 2611.9 | X | X | <1.30 |
| 2625.7 | X | X | <1.24 |
| 3868.8 | X | X | X |
| 3889.1 | X | X | X |
| 42021012 | | | |
| 2364.8 | X | X | <0.99 |
| 2395.6 | X | X | <0.91 |
| 2611.9 | X | X | <0.81 |
| 2625.7 | 5 ±60 | 168 ±60 | −1.38 ±0.44 |
| 3868.8 | 112 ±34 | 79 ±34 | −0.92 ±0.33 |
| 3889.1 | X | X | X |
| SDSS K+A Galaxies | | | |
| J212043 | | | |
| 2364.8 | ... | ... | ... |
| 2395.6 | ... | ... | ... |
| 2611.9 | ... | ... | ... |
| 2625.7 | −8 ± 20 | 83 ±20 | −1.19 ±0.26 |
| 3868.8 | ... | ... | ... |
| 3889.1 | ... | ... | ... |
| J215518 | | | |
| 2364.8 | ... | ... | ... |
| 2395.6 | ... | ... | ... |
| 2611.9 | X | X | <0.97 |
| 2625.7 | 85 ± 54 | 224 ±51 | −2.82 ±0.57 |
| 3868.8 | ... | ... | ... |
| 3889.1 | ... | ... | ... |

[a]'X' indicates spectral coverage of this line but no significant emission. $2\sigma$ upper limits are given for the EW in these cases.
[b]'...' indicates no spectral coverage of this line.

In this section we discuss our results, including the prevelance and properties of outflowing galactic winds in AGN host galaxies and post-starburst galaxies at intermediate redshift, the driving mechanism of the winds, and the implications for star formation quenching.

### 6.1. *Prevalence of Winds*

Table 8 provides a summary of the objects in our sample, their location in the restframe optical color-magnitude diagram, and an indication of which objects have outflowing winds detected in blueshifted Mg II and Fe II absorption and detections of Mg II emission and/or Fe II* emission. We find blueshifted absorption indicative of an outflow in six of our ten X-ray AGN host galaxies and four of our thirteen K+A galaxies, 43% of our full sample. For all of these galaxies, blueshifted absorption is detected in Mg II; some galaxies additionally show blueshifted absorption in either Fe II or Mg I. We find evidence for winds in galaxies across the color-magnitude diagram, including one X-ray AGN host galaxy on the red sequence. These results are shown graphically in Figure 1. We note that these are galactic-scale winds, as the observed covering fraction is high and for the galaxies with AGN, the AGN does not dominate the galaxy continuum light; therefore the background light source is extended.

We additionally find that most of the galaxies in our sample show line emission in either Mg II or Fe II*. While this emission may be from the wind itself, it is difficult to extract kinematic information about possible outflows as the emission is isotropic and is observed summed over the entire galaxy. Therefore symmetry washes out kinematic information along a given sightline, unlike in the case of absorption. Five of the ten X-ray AGN host galaxies and six of the thirteen K+A galaxies have Mg II emission. If the emission is from the wind itself, then taken together, nine of the ten X-ray AGN host galaxies and nine of the thirteen K+A galaxies, or 78% of the full sample, have winds detected either in Mg II absorption or emission. All three of the X-ray AGN host galaxies that are on the red sequence show Mg II emission, though this emission is detected only after removing the absorption due to stellar continuum in the observed spectra and therefore should be treated with caution. We do not find a strong correlation between blueshifted absorption and Mg II emission; while three galaxies in our sample have both, the rest do not. The presence of emission can fill in absorption features, however, and we emphasize that we are reporting only absorption and emission that are detected with high significance. Object 32003698, for example, has narrow blueshifted absorption in both Mg II lines, but the EW of the absorption is not significant in the presence of the strong Mg II emission in this galaxy.

Fe II* emission is detected in 50% of the X-ray AGN host galaxies and 46% of the K+A galaxies. If the Fe II* emission also originates in the wind, then a total of 100% of our X-ray AGN host sample and 77% of our K+A sample has either blueshifted absorption or line emission from a wind. As seen in Table 8, roughly half of the galaxies with blueshifted absorption also have Fe II* emission, but some objects with Fe II* emission do not have blueshifted absorption. There is also very little correlation between detection of Mg II emission and Fe II* emission. However, given that Fe II* emission is detected in K+A galaxies that do not have on-going star formation or nebular lines, it is likely that the Fe II* emission is from the wind itself. The fact that we do not often detect both Mg II and Fe II* emission in the same galaxy may be due to dust in the galaxy.

TABLE 8
Summary of Detections in Each Galaxy

| Object | Color | Blueshifted absorption | Mg II emission | Fe II* emission |
|---|---|---|---|---|
| DEEP2 X-ray AGN Host Galaxies | | | | |
| 11046507 | blue | O[1] | O | O |
| 12016790 | blue | O | X | O |
| 13004312 | red | O | O | X |
| 13025528 | green | X | O | X |
| 13041622 | blue | O | X | X |
| 13043681 | red | X | O | X |
| 13051909 | red | X | O | X |
| 13063597 | blue | X | X | O |
| 13063920 | blue | O | X | O |
| 22029058 | blue | O | X | O |
| DEEP2 K+A Galaxies | | | | |
| 31046744 | green | O | X | O |
| 32003698 | green | X | O | O |
| 32008909 | green | X | X | X |
| 41057700 | blue | X | X | X |
| 42020386 | blue | O | X | O |
| 42021012 | blue | X | X | O |
| 43030800 | green | X | O | X |
| SDSS K+A Galaxies | | | | |
| J022743 | blue | O | O | X |
| J210025 | green | X | O | X |
| J212043 | green | X | O | O |
| J215518 | green | X | O | O |
| J224603 | green | X | X | X |
| J225656 | green | O | X | X |

[a]An 'O' indicates a detection while an 'X' indicates no detection.

We find that outflows are common both in galaxies that host low-luminosity AGN and in post-starburst galaxies that are no longer forming stars. The prevalence of winds as detected in blueshifted absorption can be used to constrain the opening angle of the outflows. As we detect blueshifted absorption in 60% of the X-ray AGN host galaxies, this implies that at least 60% of these galaxies have a wind (if it is isotropic) or 100% of these galaxies could have a wind with a geometric covering fraction of 60%, corresponding to an opening angle of 66 degrees for a biconical outflow. In the post-starburst sample we detect blueshifted absorption in 29% of the DEEP2 K+A galaxies and 33% of the SDSS K+A galaxies, implying a geometric covering fraction of at least ∼30%, which corresponds to an opening angle of 46 degrees. Larger sample sizes with higher S/N would, of course, be preferable for determining these fractions and constraining wind models, as the prevalence found here is a lower limit due to the low S/N of our data.

### 6.2. *Wind Properties*

From measurements of blueshifted absorption we can constrain the minimum covering fraction and the veloc-

ities of the outflowing winds. The maximum depth of the absorption reflects the covering fraction for optically thick lines, in that it is an indication of the fraction of photons that have been absorbed and therefore the fraction of the galaxy that is covered by the wind. However, as our spectral resolution is not high, an absorption feature that is 'black' (fully absorbed) may appear to have a lower covering fraction due to the poor velocity resolution. Therefore we can measure only a lower limit on the covering fraction. As indicated in Table 5, the minimum covering fraction (equal to $A_{flow}$) of Mg II ranges from ∼0.1–0.5 in the X-ray AGN host galaxy sample and ∼0.2–1.0 in the K+A sample. Given the lower S/N of the K+A sample, we may not have been able to detect weaker absorption features in our data. As discussed in Section 4.1, the covering fraction of Fe II is similar to that of Mg II. The minimum line depth of Mg I is higher, which would indicate a lower covering fraction (∼0.1–0.2) if the line is saturated. However, for Mg I we do not know if this is the case; therefore the difference in line depth may reflect either a lower covering fraction or a lower optical depth. As the ionization potential of Mg I is 7.6 eV, much of the Mg in the wind is likely ionized, which would lead to a lower covering fraction of Mg I compared to Mg II. In that case, the Mg I that survives would likely be in dense clumps with a lower covering fraction.

The velocity centroids of the outflows detected in blueshifted absorption are typically $\sim -200 - -300$ km s$^{-1}$. The velocity widths are generally unresolved, ∼100–300 km s$^{-1}$. One AGN host galaxy has a velocity centroid of $\sim -600$ km s$^{-1}$ and a width of ∼270 km s$^{-1}$, and another AGN host galaxy has a centroid of $\sim -600$ to $-1200$ km s$^{-1}$ with a width of ∼500 km s$^{-1}$. The absorption EWs vary from ∼0.2 – 3 Å. The maximum velocity to which we detect absorption is typically ∼-400 to -800 km s$^{-1}$. We do not find a correlation between the outflow properties (velocity centroid, velocity width, EW, covering fraction) and the optical color of the galaxy or the fraction of young (<2 Gyr) stars. We detect outflows only in galaxies in which the younger stars (<2 Gyr) have ages less than 700 Myr, but given the upper limits on the non-detections this is not a particularly strong constraint. Our sample does not cover a wide enough range in X-ray luminosity to test for a dependence between outflow properties and X-ray luminosity.

### 6.3. *Comparison With Other Samples*

The sample we present here is quite complementary to other samples with measured wind properties from Mg II absorption at $z \sim 0.5 - 1$. Weiner et al. (2009) and Rubin et al. (2010) present results for typical star-forming galaxies at $z \sim 1$, selected from flux-limited galaxy samples. Both studies find that star-forming galaxies at these redshifts commonly have outflows with velocity centroids of $\sim 200-300$ km s$^{-1}$, with absorption seen out to $\sim 800$ km s$^{-1}$. Our results here for winds in X-ray AGN host galaxies and K+A galaxies are very similar, even though our galaxy samples are selected differently.

Our detection of Mg II winds in X-ray AGN host galaxies that are on the red sequence is somewhat analogous to results from Sato et al. (2009), who study Na D absorption in lower redshift galaxies in AEGIS, at $z \sim 0.1-0.5$. They find that many red sequence galaxies have winds in Na D (see their Fig. 10) with velocities $\lesssim 200$ km s$^{-1}$ (though stellar absorption was not removed). They note that many of the red sequence galaxies with winds show signs of recent star formation, however, which may indicate a correlation between the wind and the quenching of star formation in these systems. More recently, Bowen & Chelouche (2011) find that Mg II absorption along QSO lines of sight around massive luminous red galaxies (LRGs) at similar redshifts is very rare, $\lesssim$10%. LRGs are expected to be at a later evolutionary stage than the red sequence galaxies studied here, however, and it is entirely possible that their assembly history and/or star formation quenching mechanism(s) are quite different than for typical red galaxies, or that the winds do not reach the combination of impact parameter and density needed for detection against background QSOs.

Our sample does not show the extreme velocity outflows seen by Tremonti et al. (2007) in their SDSS post-starburst sample at $z \sim 0.6$, except for one X-ray AGN host galaxy that appears to have an outflow with a velocity centroid $\gtrsim$600 km s$^{-1}$. Compared to the Tremonti et al. (2007) K+A galaxies, the post-starburst galaxies that we study are more common and less luminous and are therefore likely to reflect a more frequent path to the red sequence. Our SDSS K+A galaxies are also redder, which may indicate that they are at a later evolutionary stage. Additionally, the absorption profile that we observe in our sample is similar to that seen in the coadded spectra of star-forming galaxies in Weiner et al. (2009) and Rubin et al. (2010), with absorption extending from systemic out to $\gtrsim -600$ km s$^{-1}$, often with a sawtooth-like profile. We do not observe profiles akin to what is seen by Tremonti et al. (2007), in which the absorption profile is narrower and offset from systemic, with very little to no absorption at systemic. It appears that either the driving mechanism or duration of the gas ejection is different between our sample and that of Tremonti et al. (2007).

Our results regarding winds in AGN host galaxies can be compared with work by Rupke et al. (2005) at lower redshift and Hainline et al. (2011) at higher redshift. At $z \sim 0.2$, Rupke et al. (2005) find that starburst, IR-bright galaxies with LINER emission have marginally higher velocity winds (∼100 km s$^{-1}$, measured with 95% confidence) than non-LINER galaxies. They find that the detection rate of winds in LINER galaxies is the same as in non-LINER galaxies and note that the LINER emission may come from shocks in the gas of the galaxy or wind, as opposed to weak AGN emission. At $z \sim 2-3$, Hainline et al. (2011) find that in UV-selected galaxies with optically-identified, narrow-line AGN, the Si IV absorption line in a coadded spectrum of 33 AGN host galaxies shows absorption at higher velocities than in a coadded spectrum of non-AGN host galaxies. However, the interpretation is complicated by the presence of Si IV emission, which is stronger in the AGN host galaxies. Emission-line filling may therefore account for the bulk of the difference observed. We conclude, therefore, that our finding that X-ray selected AGN host galaxies at $z \sim 0.2-0.5$ do not have significantly faster winds than star-forming galaxies at similar redshifts is not strongly at odds with results from lower and higher redshift.

### 6.4. *Implications for Wind Models and Star Formation Quenching*

What is the physical driver of the winds detected here? For sources in our AGN host galaxy sample, given that their wind properties are similar to those in our K+A sample and in the star-forming samples of Weiner et al. (2009) and Rubin et al. (2010), we conclude that the winds are not primarily AGN-driven. The fact that whether or not a galaxy has a low luminosity AGN does not change its wind properties suggests that the winds are driven by supernovae. The relatively low outflow velocities observed are consistent with this scenario, though it is possible that low luminosity AGN drive winds with comparable velocities as those observed in star-forming galaxies. However, for the X-ray AGN host galaxies that have ongoing star formation, SNe-driven winds seem quite plausible. We also note that as these galaxies are continuing to form stars, the AGN in them can not have driven such strong winds so as to have quenched star formation. Four of the six blue X-ray AGN host galaxies studied here also show Mg II and/or Fe II absorption at the systemic velocity of the galaxy, indicating that the winds in these galaxies have not fully expelled the cool gas present. The LIRG in our sample lies on the lower-redshift relation of Martin (2005) for wind velocity versus SFR (the LIRG has a SFR of 45 $M_{\odot} yr^{-1}$, estimated from the 24$\mu$m flux), implying consistency with a SNe-driven wind. For the red X-ray AGN host galaxies in our sample with winds, the winds may be relic winds that were driven by SNe during the quenching of star formation in these galaxies.

If the winds in the X-ray AGN host galaxies are nonetheless driven by the AGN itself and not SNe, we note that the wind velocities are not particularly high, indicating that low luminosity AGN are unlikely to drive strong enough winds to quench star formation. Whether the winds are due to either star formation (at least in the blue galaxies) or low luminosity AGN activity, the outflows observed do not appear to be fast enough to clear the ISM of the galaxy and lead to migration to the red sequence. Weiner et al. (2009) estimate the escape velocities of their $z \sim 1.4$ star-forming DEEP2 galaxies using the O II 3727 Å linewidth and find that the median escape velocity is ∼400-450 km s$^{-1}$ for galaxies with stellar masses log(M)∼9.5-10.5 $M_{\odot}$ and SFR∼10-40 $M_{\odot}$ yr$^{-1}$. The velocity centroids of the winds we detect in our sample are generally lower than this estimated escape velocity, though the maximum velocity observed for many of our sources (especially the AGN hosts) does exceed this. This implies, similarly to the Weiner et al. (2009) sample, that while some of the gas may be travelling at high enough speeds to escape the halo of the galaxy, the bulk of the gas remains bound.

Winds in the post-starburst galaxies studied here may be driven by SNe resulting from the most recent starburst. It is worth noting that several of our K+A galaxies have Mg II and/or Fe II absorption at the systemic velocity. These galaxies, which are either in the blue cloud or green valley, apparently have cool gas that was not expelled either during the recent starburst or by the current outflowing wind. Why do we not observe extreme outflows similar to those observed by Tremonti et al. (2007)? Our K+A galaxies may be at a later evolutionary stage, which could suggest that the extreme wind phase, if present, does not last long. However, if our K+A galaxies are at a later evolutionary stage and further on their way to the red sequence, and if the extreme outflows only exist in the youngest objects, our objects should have already gone through the extreme wind phase. As our objects are still in the process of ejecting gas, this scenario would require that they had a wind with a central velocity > 1000 km s$^{-1}$ which nonetheless did not clear the ISM from the galaxy. A more plausible explanation is that these sources have not passed through the extreme wind phase observed by Tremonti et al. (2007). Either these galaxies have not had a violent AGN outburst, or if the winds in the Tremonti et al. (2007) sources are SNe-driven and not AGN-driven, then perhaps the recent starburst in the K+A galaxies in our sample did not form as many stars as those in the Tremonti et al. (2007) sample and as such there are fewer SNe driving winds in our galaxies. Preliminary evidence from the Tremonti et al. (2007) sample indicates that the starburst decay time – or timescale for star formation quenching – is extremely short in those galaxies (∼25 Myr, Tremonti, private communication), which implies that they are not 'typical' post-starburst galaxies.

It is notable that the one object in our sample that may have an extreme wind with a velocity >1000 km s$^{-1}$ is an X-ray AGN host galaxy on the red sequence. We note that if the wind was launched 640 Myr ago (corresponding to the age of the young stellar population in this galaxy) and has been traveling at a constant speed of ∼1,000 km s$^{-1}$ since, it would now be at a radius of ∼650 kpc and would likely not be observable in absorption. This argues that the wind was either launched more recently or (possibly more likely) has not been traveling at this high constant velocity since its inception. If this wind is a relic AGN wind, then it may be that the AGN was powerful enough to drive a wind that shut off star formation in this red galaxy. If this is the case and is common for AGN in red host galaxies, then the AGN observed in blue host galaxies may be intrinsically different (e.g., have lower mass black holes, lower accretion rates, and/or be at an earlier evolutionary stage) and therefore drive lower velocity winds. We note, however, that only one of the three red AGN host galaxies studied here has a wind detected in absorption for which we can derive kinematic information.

In summary, we find in our sample targeting low-luminosity AGN host galaxies and post-starburst galaxies at intermediate redshift that outflowing galactic winds are prevalent in these galaxies, as detected either by Mg II and Fe II absorption or Mg II and Fe II* emission. The velocities of the winds are roughly consistent with those observed in star-forming galaxies at similar redshifts. Further, the presence of a low-luminosity AGN does not appear to commonly drive faster winds, such that these winds are likely SNe-driven. In our post-starburst sample we do not detect the extreme winds observed by Tremonti et al. (2007) and conclude that most post-starburst galaxies likely do not host such high velocity winds. We therefore find that while galactic winds are common in both low-luminosity AGN host galaxies and post-starburst galaxies, they do not appear to play a major role in quenching star formation.

The authors would like to thank Aleks Diamond-Stanic, Katherine Kornei, Crystal Martin, John Moustakas, Jason X. Prochaska, Kate Rubin, Alice Shapley, and Christy Tremonti for useful discussions. We also thank Christy Tremonti for sharing her stellar continuum fitting code. The data presented herein were obtained at the W.M. Keck Observatory, which is operated as a scientific partnership among the California Institute of Technology, the University of California and NASA. The Observatory was made possible by the generous financial support of the W.M. Keck Foundation. The authors wish to recognize and acknowledge the very significant cultural role and reverence that the summit of Mauna Kea has always had within the indigenous Hawaiian community. The Keck access used for these observations is from NOAO and the University of California. This study uses data from both the AEGIS survey, which is supported in part by the NSF, NASA, and the STFC, and the SDSS survey, which is supported in part by the Alfred P. Sloan Foundation, the participating institutions, the NSF, the U.S. Department of Energy, and NASA.

## REFERENCES

Bell, E. F., et al. 2004, ApJ, 608, 752
Best, P. N., Kaiser, C. R., Heckman, T. M., & Kauffmann, G. 2006, MNRAS, 368, L67
Binney, J. 2001, in Astronomical Society of the Pacific Conference Series, Vol. 250, Particles and Fields in Radio Galaxies Conference, ed. R. A. Laing & K. M. Blundell, 481
Blanton, M. R., & Roweis, S. 2007, AJ, 133, 734
Blanton, M. R., et al. 2003, ApJ, 594, 186
Bowen, D. V., & Chelouche, D. 2011, ApJ, 727, 47
Bower, R. G., et al. 2006, MNRAS, 370, 645
Brown, M. J. I., et al. 2007, ApJ, 654, 858
Bruzual, G., & Charlot, S. 2003, MNRAS, 344, 1000
Bundy, K., et al. 2006, ApJ, 651, 120
Cattaneo, A., et al. 2007, MNRAS, 377, 63
Chen, Y., et al. 2010, AJ, 140, 445
Coil, A. L., et al. 2009, ApJ, 701, 1484
Croton, D. J., et al. 2006, MNRAS, 365, 11
Dale, D. A., & Helou, G. 2002, ApJ, 576, 159
Davis, M., Newman, J. A., Faber, S. M., & Phillips, A. C. 2000, in Proceedings of the ESO/ECF/STSCI Workshop on Deep Fields, Garching (Publ: Springer)
Davis, M., et al. 2003, Proc. SPIE, 4834, 161
—. 2007, ApJ, 660, L1
Dressler, A., & Gunn, J. E. 1983, ApJ, 270, 7
Faber, S. M., et al. 2007, ApJ, 665, 265
Goto, T. 2007, MNRAS, 377, 1222
Hainline, K. N., Shapley, A. E., Greene, J. E., & Steidel, C. C. 2011, ApJ, in press
Heckman, T. M., Lehnert, M. D., Strickland, D. K., & Armus, L. 2000, ApJS, 129, 493
Hopkins, P. F., et al. 2005, ApJ, 630, 705
Kriek, M., et al. 2008, ApJ, 682, 896
Laird, E. S., et al. 2009, ApJS, 180, 102
Lehmer, B. D., et al. 2010, ApJ, 724, 559
Lin, L., et al. 2007, ApJ, 660, L51
Martin, C. L. 2005, ApJ, 621, 227
Martin, C. L., & Bouche, N. 2009, ApJ, 703, 1394
Morton, D. C. 2003, ApJS, 149, 205
Oke, J. B., et al. 1995, PASP, 107, 375
Ostriker, J. P., & Ciotti, L. 2005, Royal Society of London Philosophical Transactions Series A, 363, 667
Park, T., et al. 2006, ApJ, 652, 610
Phillips, A. C. 1993, AJ, 105, 486
Phillips, A. C., Miller, J., Cowley, D., & Wallace, V. 2008, in Presented at the Society of Photo-Optical Instrumentation Engineers (SPIE) Conference, Vol. 7014, Society of Photo-Optical Instrumentation Engineers (SPIE) Conference Series
Pickles, A. J. 1998, PASP, 110, 863
Prochaska, J. X., Kasen, D., & Rubin, K. 2011, ApJ, in press
Quintero, A. D., et al. 2004, ApJ, 602, 190
Rieke, G. H., et al. 2009, ApJ, 692, 556
Rodríguez-Merino, L. H., et al. 2005, ApJ, 626, 411
Rubin, K. H. R., et al. 2010, ApJ, 719, 1503
—. 2011, ApJ, 728, 55
Rupke, D. S., Veilleux, S., & Sanders, D. B. 2005, ApJS, 160, 115
Sanders, D. B., et al. 1988, ApJ, 325, 74
Sato, T., et al. 2009, ApJ, 696, 214
Shapley, A. E., Steidel, C. C., Pettini, M., & Adelberger, K. L. 2003, ApJ, 588, 65
Steidel, C. C., et al. 2010, ApJ, 717, 289
Strateva, I., et al. 2001, AJ, 122, 1861
Thacker, R. J., Scannapieco, E., & Couchman, H. M. P. 2006, ApJ, 653, 86
Tremonti, C. A., Moustakas, J., & Diamond-Stanic, A. M. 2007, ApJ, 663, L77
Veilleux, S., Cecil, G., & Bland-Hawthorn, J. 2005, ARA&A, 43, 769
Weiner, B. J., et al. 2009, ApJ, 692, 187
Willmer, C. N. A., et al. 2006, ApJ, 647, 853
Yan, R., et al. 2009, MNRAS, 398, 735
Yang, Y., et al. 2008, ApJ, 688, 945
York, D. G., et al. 2000, AJ, 120, 1579
Zabludoff, A. I., et al. 1996, ApJ, 466, 104